Characterisation of supersonic turbulent combustion in a Mach-10 scramjet combustor

Augusto F. Moura *, Nicholas Gibbons†, Vincent Wheatley‡, Timothy McIntyre§ and Ingo Jahn¶
The University of Queensland, Brisbane, Australia, 4072

Turbulent combustion remains an unsolved problem and the simulation models that have been developed, while accurate for subsonic turbulent combustion, have limited accuracy when applied to supersonic combustion. An experiment has been developed to characterise supersonic turbulent combustion in a geometrically simple flow-path that is capable of accurately reproducing the complex and highly non-uniform flow structures present in flight-candidate scramjet engines. An inlet-fuelled scramjet engine was designed with a symmetrical intake to reproduce the correct flow structures. This was tested with an inflow condition of Mach 7, using a Mach-10 flow enthalpy of 4.6 MJ/kg to reproduce the combustion conditions in a flight vehicle operating at Mach 10. The turbulent flame was directly observed in the flow using planar laser-induced fluorescence of OH radicals. These results have been complemented by Large-Eddy Simulations of the experimental conditions, showing that the combustion process in scramjets is multi-mode, where neither premixed nor non-premixed combustion dominates, and both substantially contribute to heat release. These modes are present simultaneously inside the engine. For both modes, combustion is confirmed to happen over multiple combustion regimes. This work provides new insight into the supersonic turbulent combustion process and enhances our understanding of combustion in scramjet engines.

Nomenclature

Da	=	Damköhler number
e	=	specific energy, J/kg
f	=	focal length, mm
$\mathbf{F}_c$	=	convective fluxes
$\mathbf{F}_v$	=	viscous fluxes
H	=	enthalpy, MJ/kg

*PhD Candidate, Centre for Hypersonics, School of Mechanical and Mining Engineering
†Research Student, Centre for Hypersonics, School of Mechanical and Mining Engineering.
‡Associate Professor, Centre for Hypersonics, School of Mechanical and Mining Engineering, AIAA Senior Member.
§Associate Professor, Centre for Hypersonics, School of Mathematics and Physics.
¶Senior Lecturer, Centre for Hypersonics, School of Mechanical and Mining Engineering, AIAA Member.

J	=	matrix of the derivatives of reaction rates divided by conserved variables
k	=	specific kinetic energy, $\mathrm{m}^2/\mathrm{s}^2$
M	=	Mach number
$\dot{m}$	=	mass flow rate, kg/s
$\hat{n}$	=	unit normal vector
p	=	pressure, Pa
Re	=	Reynolds number
S	=	cell face area, m^2
T	=	temperature, K
t	=	time, s
TFI	=	Takeno Flame Index
U	=	conserved variables
u	=	velocity in the x direction, m/s
V	=	cell volume, m^3
v	=	velocity in the y direction, m/s
ν_t	=	turbulent viscosity, m^2/s
w	=	velocity in the z direction, m/s
$\dot{w}$, $\overline{W}$	=	source terms
Y	=	mass fraction
Δ	=	LES filter
ϵ	=	specific turbulent dissipation, $\mathrm{m}^2/\mathrm{s}^3$
ϕ	=	fuel equivalence ratio
ρ	=	density, $\mathrm{kg/m}^3$
τ	=	time scale, s

Subscripts

c	=	chemical
r	=	resolved scales
s	=	nozzle supply
sgs	=	subgrid scales
t	=	turbulent

I. Introduction

Scramjet engines are the best-suited engine cycle for hypersonic flight and present several advantages over rocket-powered vehicles [1–4], which makes them promising replacements for rockets in access-to-space systems. One application currently under investigation consists of a scramjet as the second stage in a three-stage-to-orbit system [1, 5]. Such a system would need a scramjet engine capable of operating at Mach numbers of up to at least ten [6]. However, overcoming the drag to achieve the positive net thrust necessary for accelerating at such flight velocities is not trivial. While sufficient thrust has been achieved in scramjets operating at lower Mach numbers through the use of empirical data and repeated testing, this hasn't been successful for the higher Mach number flight conditions necessary for accelerating vehicles [7]. A better understanding of the underlying physical processes is necessary to design higher-efficiency engines from the ground up.

Of particular interest to this work is the supersonic turbulent combustion process. A combustion efficiency of at least 80% is required for an access-to-space scramjet system. This is not easily achievable in high-velocity scramjet flows [8]. The physics of supersonic turbulent combustion are not fully understood [9–11]. Models exist that adequately reproduce subsonic turbulent combustion. Their adequacy is, however, limited or uncertain for its supersonic counterpart. Many experimental and numerical investigations of supersonic combustion, focusing primarily on direct-connect combustors, have demonstrated that combustion in scramjets may happen over a wide range of regimes [12–19].

One of the most relevant supersonic combustion experiments in scramjets is the work performed by [16, 17]. The experiments consisted of a combustor with a shock generator to try and reproduce realistic scramjet combustor conditions. The configuration consisted of a 75-mm wide combustor with a height of 15 mm. It has a 10° shock generator at the inlet. A single injector with a diameter of 2 mm is situated 70 mm from the leading edge at the center plane. The shock generator was introduced to create a shock train and mimic the structures seen in scramjet engines. The model is equipped with ample optical access and OH-PLIF was used to visualise the flame structure along the entire combustor. The experiment was performed in an expansion tube with free-stream conditions of approximately $p = 40$ kPa, $T = 1200$ K, and $M = 2.8$. Fuel equivalence ratios of 0.08, 0.23 and 0.44 were tested.

The results indicate that reactions take place at the edge of the fuel plume, along thin reaction sheets or flamelets, for every case. Thicker reaction zones are present only in the highest equivalence ratio case where the fuel plume hits the opposite wall, resulting in boundary-layer burning. This seems to indicate there is little mixing and fuel immediately burns as it gets in contact with the air around the fuel plume. This is likely due to the flow conditions around the injector being sufficient for hydrogen autoignition, as the free-stream conditions themselves are close to the required conditions [20]. The conditions behind the oblique shock from the 10° shock generator, where the injector is located, are even higher. While these conditions are not quoted in the paper, estimating with oblique-shock relations would give $p \approx 80$ kPa and $T \approx 1470$ K, which are well above the 50 kPa/1000 K requirement for hydrogen autoignition.

These are relevant experiments but seem to be limited in how representative they are of combustion in a flight vehicle-integrated scramjets. The shock structure created by the 10° ramp is rather weak, with a contraction ratio of 1.5, whereas scramjet inlets usually present higher contraction ratios and stronger shocks. While this work is much better in capturing realistic flow structures than the uniform direct-connect inflow used in most other experiments, the shocks are still arguably not strong enough to create the non-uniformities expected in scramjets. Furthermore, it is not representative of inlet-injected scramjets, where the fuel is injected on the inlet ramps into a flow that is still not fully compressed. With inlet injection, the extra length gives the fuel more time to mix before burning, which could change the flame structure and consequently regimes. As discussed in the previous paragraph, the flow around the injector in the experiment is very hot and with high pressure. This most likely causes extremely mixing-limited combustion, leading to the observed localised reactions in thin zones. A complete, inlet-fuelled scramjet engine would provide more realistic flow conditions than a simplified model. Finally, and perhaps most importantly, there is no characterisation of the combustion regimes in the model combustor, which is of vital interest to provide better data for the development of combustion models.

To summarise, the available literature on supersonic combustion has its limitations. Direct-connect experiments generate highly uniform flow, unlike the flow in an airframe-integrated, real scramjet engine, where intake shocks drive ignition, amplifying flow non-uniformities and turbulence, and produce severe non-uniformities in the combustor. Investigation of streamwise vortex-oblique shock interactions has shown that there is a massive amplification of the unsteadiness [21], and the oblique shocks amplify non-uniformities. This means the strong intake shocks in scramjets play a critical role in the flow structures and therefore combustion processes. On the other hand, even the addition of shock generators to the direct-connect combustors is usually not enough to produce such a strong shock train in the combustor conditions investigated with Mach numbers usually less than four. Experimental work focusing on determination of combustion regimes is nearly non-existent. Furthermore, Large-Eddy Simulations performed on a previous experimental scramjet tested in the T4 Reflected Shock Tunnel at The University of Queensland have shown that the range of regimes may in fact be wider than suggested [22]. To address this lack of engine-representative combustion data, a complete scramjet engine was designed, to be tested at flow enthalpy conditions equivalent to flight at Mach 10. Flame visualisation is performed with planar laser-induced fluorescence of OH radicals (OH-PLIF). The engine was designed to be simple to simulate, while capturing the key flow features of a real scramjet, allowing for high-fidelity Large-Eddy Simulations (LES) of the flow field to complement the experimental results and to fully characterise the supersonic turbulent combustion process present in real scramjet engines.

II. Methodology

A. Experimental facility and model

The experimental results in this work were obtained in the T4 Reflected Shock Tunnel at The University of Queensland. T4 is a free-piston-driven shock tunnel, in which the work from a piston is used to create the hypersonic, high-enthalpy conditions in the test section [23]. The Mach 7.6 nozzle was used to generate the conditions shown in Table 1. These conditions are the averaged experimental conditions for all experimental tests, or "shots" as they're commonly referred to, and are calculated using NENZFr [24], an internally developed code at the Centre for Hypersonics. It uses the nozzle supply conditions calculated with ESTCj [25] and couples it with 2D axisymmetric RANS simulations of the nozzle, done with the Eilmer 3 code [26, 27], to determine the nozzle exit flow conditions. Eilmer 3 was developed to solve the three-dimensional Navier-Stokes equations for turbulent chemically-reacting compressible flows. While this condition has an inflow Mach number of 7.4, the enthalpy is 4.6 MJ/kg, which is equivalent to a Mach-10 flight condition. This is to reproduce the combustion characteristics of a Mach 10 flight vehicle. The model is therefore tested in semi-freejet mode, meaning the inflow condition for the model is the same as the conditions behind a weak forebody shock in Mach-10 flight. The presence of O and NO species in the free-stream is an unavoidable consequence of the way T4, and reflected shock tunnels in general, operate. The flow that supplies the nozzle is generated through a reflected shock (hence the facility name), which creates a stagnation region of extremely high pressure and temperature. In this region, air dissociates, producing these species. As the flow expands over the nozzle the chemistry is frozen, meaning these species are present in ground test flows.

Table 1 Experimental free-stream conditions.

H_s	[MJ/kg]	4.63	±	7.3%
p_∞	[Pa]	3056	±	3.7%
T_∞	[K]	417	±	8.3%
u_∞	[m/s]	2986	±	3.2%
ρ_∞	kg/m^3	0.026	±	5.9%
M_∞	-	7.4	±	1.9%
$Y_{N_2,\infty}$	-	0.735	±	0.4%
$Y_{O_2,\infty}$	-	0.195	±	2.2%
$Y_{NO,\infty}$	-	0.068	±	10%
$Y_{O,\infty}$	-	0.0016	±	39%

The experimental model is shown in Fig. 1. The model was designed to experimentally reproduce a complete scramjet engine flow path with intake ramps, while still being geometrically simple enough to facilitate analysis and simulation of the flow path. This was achieved by designing an engine that is symmetric along its horizontal plane, with a rectangular combustor 400-mm long and 16-mm high. The intake is composed of two ramps, a forebody and a ramp with 6° and 15°, respectively (6° and 9° turning angle). The sidewalls begin at the 9° ramp, with an engine width of

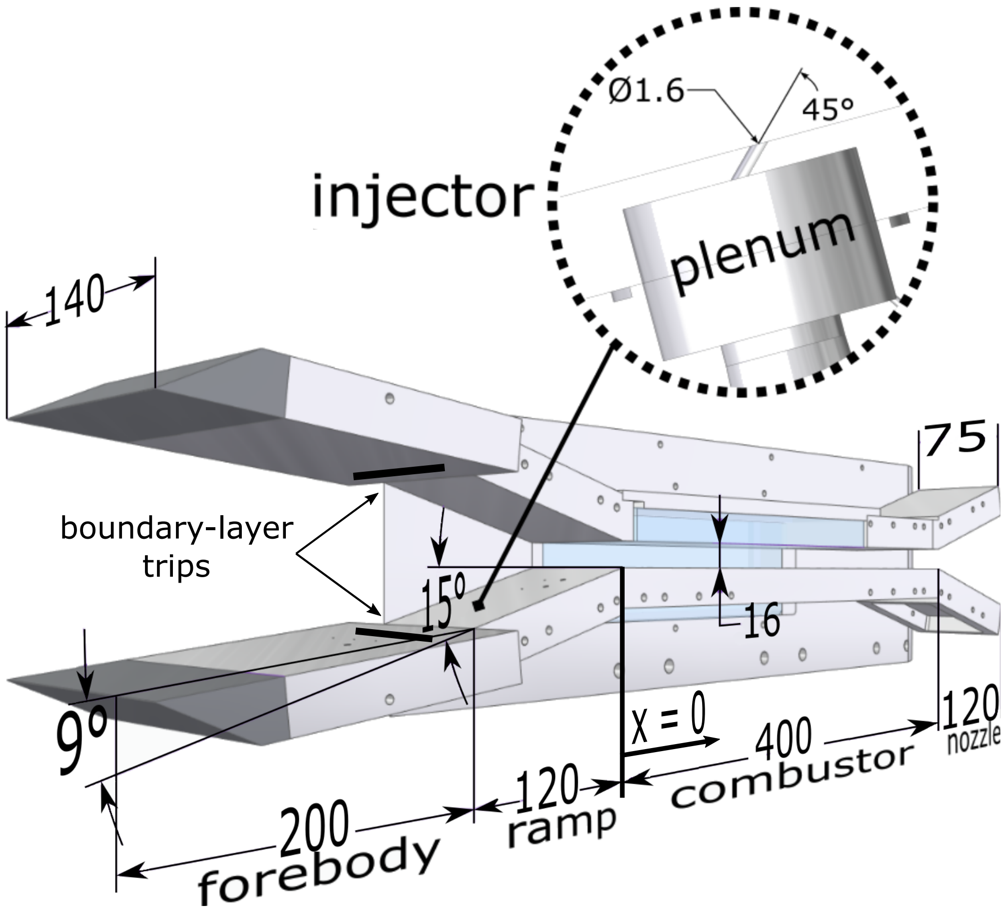

Fig. 1 Schematic of the experimental engine model. The closest sidewall is removed to allow visibility of the internal flow path. Dimensions are in mm.

75 mm. The forebody is wider and without sidewalls to prevent edge effects from being ingested by the engine. For fuelling, there is a single 1.6-mm diameter injector located along the vertical center plane on the lower ramp, 80 mm upstream from the combustor entrance, or throat ($x = 0$). The injector is angled at 45° to the ramp to which it is attached. The single injector ensures the engine is simpler to analyse and simulate. It produces a single fuel plume which, at the test fuel equivalence ratio of around 0.13, never interacts with either the sidewalls or the opposite combustor wall. This allows for easier LES simulations because it reduces the cell density requirement closer to the walls, reducing overall computational cost.

The experimental model is equipped with boundary-layer trips on the forebody ramps, about 10-mm upstream of the corner between the ramps. Their position is indicated in Fig. 1. Trips were required on the experimental model due to the impulsive nature of the tests. Without trips, a large separation formed near the injector, leading to engine unstart. The added turbulence from the trips prevented this from happening. The effects of the trips are discussed in more detail in Section III.

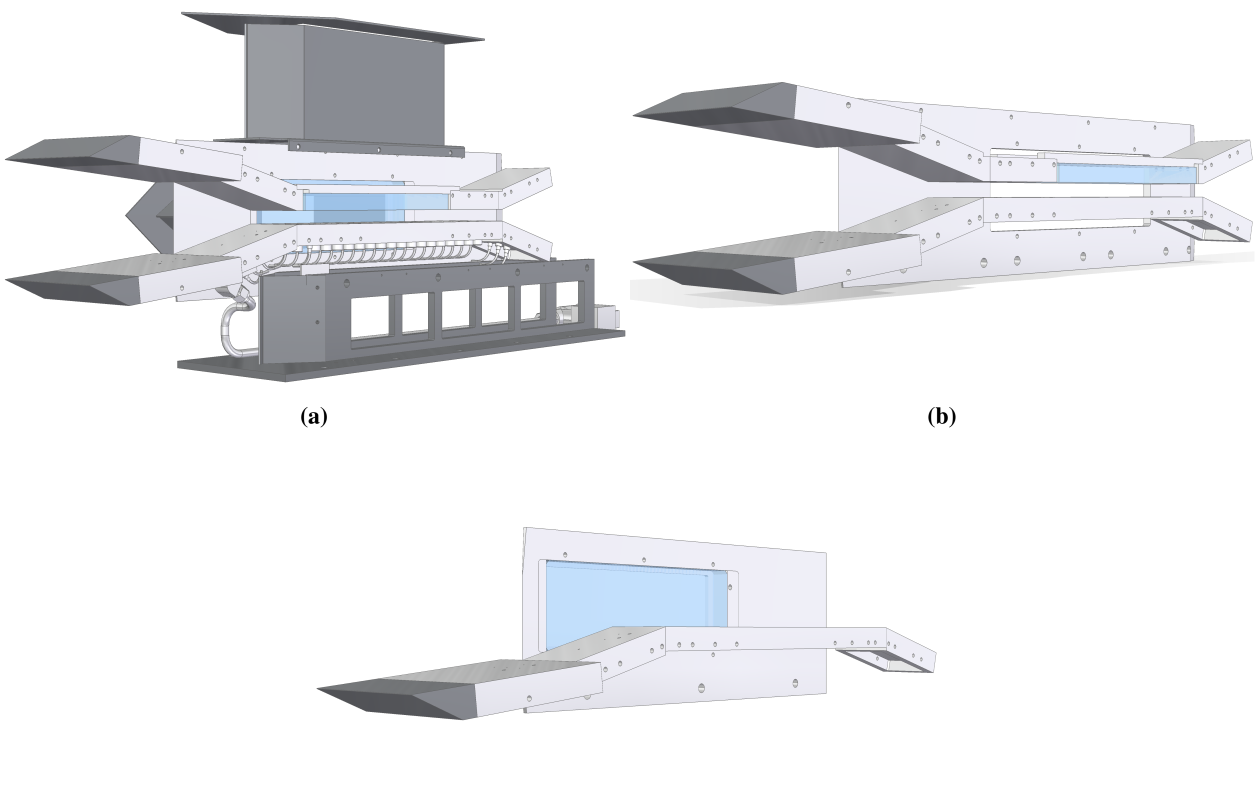

(a) **(b)**

(c)

Fig. 2 Configurations of the experimental engine. (a) Combustor front, (b) combustor rear and (c) injector only, allowing OH-PLIF visualisation of each region respectively.

The engine model is reconfigurable so that flow visualisation can be performed from the injector to the end of the combustor and instrumented with pressure sensors on the lower wall (see Section II.A.1). Three configurations are

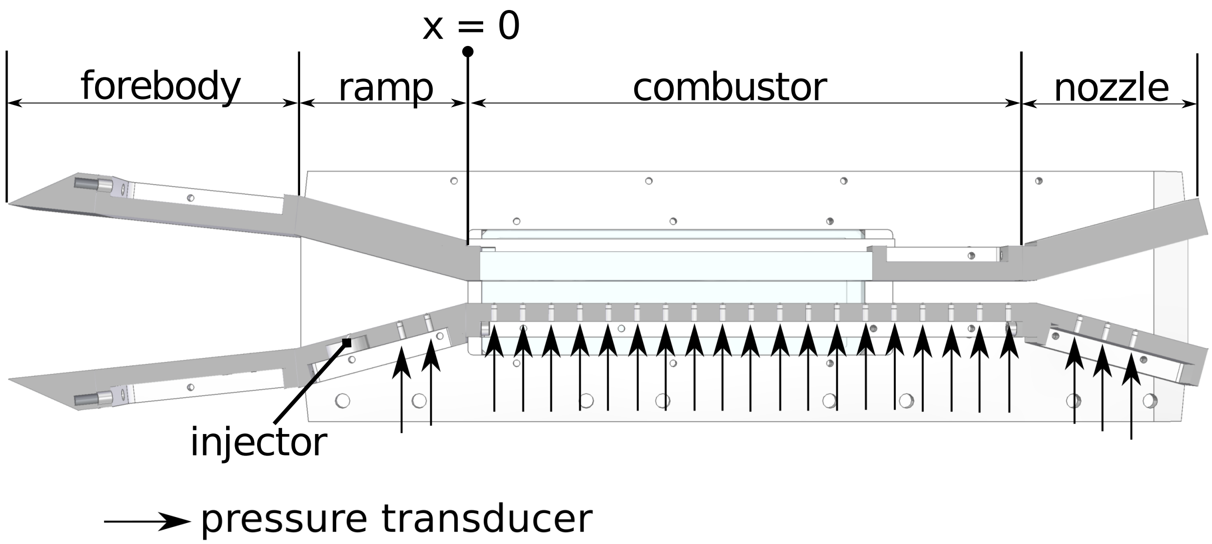

Fig. 3 Schematic of the experimental model with position of the pressure transducers.

used to achieve this, which can be seen in Fig. 2. The closest sidewall has been removed to allow visualisation of the internal flow path. Figure 2a retains the optical path shielding and mounting structure, which are not present in the other configurations for clarity. All three configurations allow for OH-PLIF and schlieren visualisation of the flow, although the latter was only done in the injector region. For the *combustor front* (CF) and *combustor rear* (CR) configurations, the full engine is used and the sidewalls are rotated 180° between configurations. This moves the window ports on the sidewalls to different parts of the combustor. The combustor wall opposite the injector is a window, which allows the laser sheet to come down into the combustor. The *injector only* (IO) configuration uses only the bottom half of the engine for visualisation of the flow around the injector upstream of the throat. The flow on each compression ramp is influenced only by the shocks on its side, as the intake shocks only interact and reflect further downstream. This means any visualisation of the region just downstream of the injector is still representative of the full engine. As only half the engine is used, pressure data in the combustor is not comparable with the other cases. Therefore, only pressure data for the ramp is obtained in this configuration. The optical configuration for the visualisation techniques is detailed in Section II.A.2.

1. Model instrumentation

The model is instrumented with pressure transducers along the walls on the injector side (lower half) from ramp to nozzle. The distribution of the sensors in the model is given in Fig. 3.

The model can be equipped with up to 26 pressure transducers. These are fast-response Kulite XTEL-190 (M) series, which measure absolute pressure with a piezo-resistive silicon sensor. All but two pressure transducers are located in the center-line of the model. The extra two transducers are parallel to the first transducer in the combustor (x = 20 mm). These are offset span-wise 20 mm to each side of the center transducer. They are used to verify if the flow entering the combustor is symmetric with respect to the center plane.

The pressure traces obtained from the sensors need to be normalised to account for the change in nozzle supply pressure over the test time and the travel time of the test gas over the model. The normalised pressure during the test time is calculated as:

$$p(t) = \frac{p(t + t_d)}{p_s(t)} \times \frac{p_{s,\mathrm{nom}}}{p_{1,\mathrm{nom}}} \tag{1}$$

where $p_{s,\mathrm{nom}}$ is the mean nozzle supply pressure, $p_{1,\mathrm{nom}}$ is the mean pressure of the first forebody sensor, and t_d is the delay between nozzle supply trigger and the trigger for each sensor, which is determined individually based on the pressure traces for the sensor. This means that the normalised signal from each sensor, time-delayed with respect to the nozzle supply pressure, is multiplied by the mean nozzle supply pressure normalised by the mean pressure in the first ramp sensor. This accounts for the small variance in conditions between shots. It also makes comparison between shots easier since all the traces from different shots start at the same normalised value $p(t) = 1$. This normalisation procedure has been successfully used before in experiments performed on T4 [28, 29].

2. Flow visualisation

Flow visualisation was performed in the experiments in the form of OH-PLIF for flame visualisation and schlieren imaging of the intake and injector. The configuration of the optical diagnostics equipment for both is described here.

The PLIF system consists of a Spectra Physics Nd:YAG pulsed laser as light source, which produces a second harmonic laser beam at 532 nm at a repetition rate of 10 Hz. This, in turn, pumps a Cobra-Stretch dye laser, using Rhodamine 6G dye to output a tuneable frequency-doubled laser beam at around 284 nm. The beam goes through a series of dichroic mirrors that direct it into the optics box above the test section. It then goes through a cylindrical lens with focal length $f = -70$ mm, which converts the beam into a laser sheet. The sheet is collimated and focused by a plano-convex lens with $f = 1000$mm. The sheet is masked to have a length of 130 mm, in order to have well-defined, sharp edges, which allows for size control and facilitates identification of the edges for normalisation of the test image. The sheet is also partially reflected with a beam splitter to a dye cell containing the Rhodamine 6G dye. A Point Grey 8-bit grey-scale camera is positioned to capture an image of the fluorescence in the dye cell. This is used to normalise the PLIF image obtained during the experiment, correcting for spatial variations in the laser sheet.

The laser sheet enters the test section through the top, going into the model through the top combustor wall, centrally-located in the span-wise direction. This excites OH molecules on a plane along the center line of the model. The emission is captured by a Princeton Instruments PIMAX 3 1024 x 1024 ICCD camera equipped with either a 25-mm or 105-mm focal-length lens. A Newport 10BPF10-310 band-pass filter with transmission wavelength of 310 ± 2 nm and FWHM 11 ± 2 nm is used to capture non-resonant fluorescence and eliminate the background radiation, including

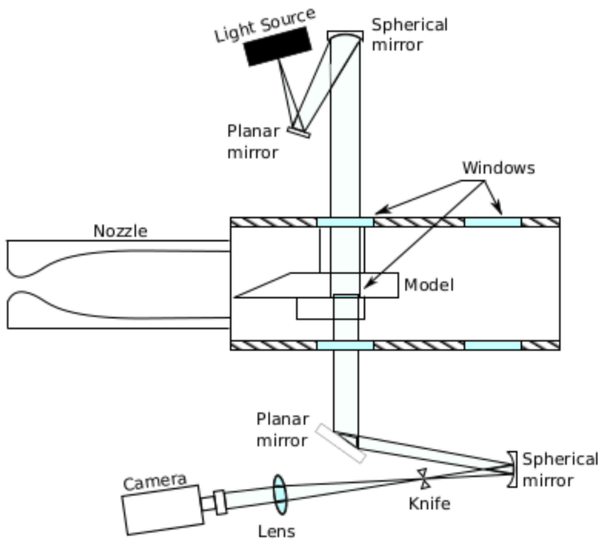

Fig. 4 Schematic of the schlieren system in T4 [21].

laser scatter, which can be more intense than the fluorescence.

The laser is tuned to a specific wavelength which needs to match an excitation transition for OH. The transition of interest is the electronic transition $A^2\sum^+ \leftarrow X^2\prod(0)$, with excitation in the $(v', v'') = (1, 0)$ vibrational band, at around 280 to 290 nm. The rotational doublet $Q_1(J'' = 9.5)$ and $Q_2(J'' = 7.5)$ was chosen, with an absorption wavelength of 283.92 nm. This doublet was chosen as the populations in these states do not change significantly over the temperature range expected in the scramjet combustor [30]. This was confirmed to match the doublet with a test scan where the laser is passed through a calibration flame.

In addition, Schlieren imaging was used to visualise the injector region and complement the OH-PLIF images obtained from this region. The schlieren configuration currently used in T4 is illustrated in Fig 4 [21]. It uses an Osram XBO 6000 W continuous xenon arc lamp as the light source. The images were recorded with a Phantom v611 high-speed camera, set in the experiments with a resolution of 400 x 800 pixels and sample rate of 13569 fps, with exposure set to 7.4×10^{-5} s. The spherical mirrors have a focal length of 2 m and the lens focusing on the camera has a focal length of 500 mm.

B. Large-Eddy Simulations

The solver used for the Large-Eddy Simulations in this work was US3D, developed at the University of Minnesota to tackle high-speed aerodynamic and aero-thermodynamic flow simulations. It solves the compressible Navier-Stokes equations using a cell-centerd finite volume scheme [31]. The solver is described briefly here.

The conservation equations, as implemented in the US3D solver, can be written in a general form:

$$\frac{\delta U}{\delta t} + \nabla \cdot (\mathbf{F}_c - \mathbf{F}_v) = \dot{w} \tag{2}$$

where $U = (\rho Y_1, ..., \rho Y_n, \rho u, \rho v, \rho w, \rho e, \rho e_v)^T$ is the vector of conserved variables, $\mathbf{F}_c$ and $\mathbf{F}_v$ represent convective and viscous fluxes and $\dot{w}$ represents the source terms [31]. In the U vector, the subscript for Y represents different species, e is energy per unit mass, e_v the vibrational energy per unit mass. Values are stored at cell centers and equations are integrated by applying the divergence theorem to the discretised transient term. The averaged rate of change of U (from Eq. 2) in each cell is the sum of the fluxes over all faces, i.e.

$$\frac{\delta \overline{U}}{\delta t} = -\frac{1}{V} \sum_{\text{faces}} [(\mathbf{F}_c - \mathbf{F}_v) \cdot \hat{n}\, S] + \overline{W}, \tag{3}$$

where V is the cell volume, S the cell face area, $\hat{n}$ the unit normal vector of the face and $\overline{W}$ are source terms. The fluxes are separated into the convective and diffusive parts, which allows for the different treatment of inviscid and viscous fluxes. The former are treated using the modified Steger-Warming method, which accounts for the high dissipation of the original method [31]. The latter are computed by averaging the gradient in adjacent cells to calculate the gradient at a cell face. Low-dissipation fluxes in smooth regions are fourth order accurate, while remaining fluxes are second order accurate in space [32]. Temporal discretisation uses the Crank-Nicolson second order accurate method, except close to the walls where the backwards Euler first order accurate method is used. The solver uses an implicit solution method combining Data-Parallel Line-Relaxation and Full-Matrix Point-Relaxation methods. A detailed explanation of the process, and of the solver as a whole, is provided by Nompelis et al. [31].

Since for wall-bound flows, such as in scramjets, the distribution of turbulent energy moves towards smaller scales closer to the walls, requiring a prohibitive increase in grid resolution to resolve these structures, the solver models the flow closer to the walls using RANS. This allows the grid resolution to be set by the LES requirements based on the free-shear flow. This hybrid RANS/LES approach, originally proposed as the Detached Eddy Simulations (DES) method, employs the density-corrected Spalart-Allmaras model one-equation turbulence model to model the flow in the near-wall regions [33–35]. The solution with this approach can be switched from RANS close to the wall to LES away from the wall by using the LES filter as a reference distance. The formulation used in this study is the Improved Delayed Detached Eddy Simulation (IDDES) [36], which introduces corrections to the modelled stress depletion of DES [37] and the log-layer mismatch of DDES (itself an initial correction of DES) [38]. This method has been validated for supersonic flows [32]. Besides the near-wall regions, modelling of the sub-grid scales is also done with the Spalart-Allmaras model in US3D. Details on the implementation of the methodology and the aforementioned corrections can be found in the references provided [36–39].

For the simulations presented here, quasi-laminar combustion was assumed, i.e. no turbulence/chemistry interaction models were used. As previously discussed, for supersonic combustion, there aren't many models available for turbulence/chemistry interactions. Studies of scramjet combustion using the assumed PDF combustion model [14] and a modified flamelet model developed for supersonic combustion [40] both found the agreement with experimental data was not improved for either model compared with quasi-laminar chemistry. On the other hand, quasi-laminar RANS simulations of a Mach-12 REST scramjet engine showed good agreement with experimental data for flow conditions similar to those investigated in this study [41].

1. Determination of combustion regimes

One of the main goals of this investigation is the determination of the combustion regimes in the scramjet combustor under the conditions analysed. The characterisation of the regimes present in the LES results was done using the methodology described below. Turbulent combustion regimes are traditionally differentiated by two non-dimensional numbers, the turbulent Damköhler and turbulent Reynolds numbers. For the Damköhler number in particular, the parameters are not trivial to obtain from the flow. The formulation used to determine these parameters and calculate the combustion regimes is explained next. The turbulent Damköhler number is given by:

$$Da = \frac{\tau_t}{\tau_c}. \tag{4}$$

where τ_t is the turbulent time scale and τ_c is the chemical time scale.

The turbulent time scale, τ_t, is determined from the turbulent kinetic energy, k_t, and the turbulent dissipation, ϵ [22]:

$$\tau_t = \frac{k_t}{\epsilon}. \tag{5}$$

The turbulent kinetic energy is determined from two components:

$$k_t = k_r + k_{sgs}, \tag{6}$$

where k_r is the resolved turbulent kinetic energy, calculated from the turbulent velocity fluctuations, and k_{sgs} is the sub-grid component, representing the energy contained in the turbulent scales that are modelled. This is calculated from the turbulent viscosity:

$$k_{sgs} = \frac{\nu_t^2}{(c_v^k \Delta)^2} \tag{7}$$

where $c_v^k = 0.07$ and Δ is the LES filter length. For more details on how these terms are obtained, see [22].

Calculation of the turbulent dissipation, ϵ, is not trivial. Wilcox [42] derived a transport equation for turbulent kinetic energy by filtering the momentum equations combining the various components. The sink terms in this transport equation can then be combined to obtain the dissipation:

$$\epsilon_r = 2\nu\overline{S'_{ij}S'_{ij}}, \tag{8}$$

where

$$S'_{ij} = \frac{1}{2}\left[\frac{\delta u'_i}{\delta x_j} + \frac{\delta u'_j}{\delta x_i}\right]. \tag{9}$$

Since there are filtered structures in the flow, Eq. 8 provides only the dissipation for the resolved energy scales. The sub-grid component is calculated from the sub-grid turbulent kinetic energy using scaling laws [22]:

$$\epsilon_{sgs} = \frac{0.931 k_{sgs}^{3/2}}{\Delta}. \tag{10}$$

As with turbulent kinetic energy, the turbulent dissipation is calculated from the resolved and filtered, or sub-grid, components:

$$\epsilon_t = \epsilon_r + \epsilon_{sgs}. \tag{11}$$

The chemical timescale, τ_c, is determined using the Chemical Explosive Mode Analysis (CEMA) [43]:

$$\tau_c = \max\left(\frac{\lambda_s + \lambda_s^*}{2}\right)^{-1}, \tag{12}$$

where λ_s represents the eigenvalues of the matrix J, which contains the derivative of each reaction rate by each conserved variable, i.e.

$$J = \frac{\delta\dot{\omega}_s}{\delta U_j}. \tag{13}$$

The term λ_s^* is a complex conjugate used to extract the real parts from the eigenvalues.
Finally, the turbulent Reynolds number is defined as:

$$Re_t = \frac{k_t^2}{\epsilon\nu} \tag{14}$$

With these parameters defined, the combustion regimes can be calculated for the solution. Since we are interested in turbulent combustion, laminar regions of the flow where there is little turbulence, or regions with negligible reaction rates, can be discarded from the analysis. To do this, the cells in the grid are filtered by turbulence level and chemical speed, i.e. cells with turbulent kinetic energy lower than 1 and reaction time higher than 1 are discarded from the analysis.

While these numbers are somewhat arbitrary, they allow filtering of the grid to remove cells where the Reynolds and Damköhler numbers offer negligible contribution to the distribution of regimes. Low turbulent kinetic energy of the order of $k_t < 1$ is much lower than the usual level of turbulence in the grid, which is of the order of 1×10^3. This leads to very low Reynolds numbers and therefore laminar flow. Similarly, a chemical time scale $\tau_c > 1$ is slower than the overall reactions by three orders of magnitude. This leads to low Damköhler numbers and therefore regions with negligible reaction rates. After the filtering, the Damköhler and Reynolds numbers are calculated for the remaining cells in the grid, and then plotted on a heat map that shows the regime distribution. These maps are shown and discussed in Section IV.C.

2. Simulation grid and boundary conditions

The computational domain for the LES simulations reproduces the flow path of the experimental model shown in Fig. 1, with a few caveats. As in the experimental model, it consists of two sets of ramps, with turning angles of 6° and 9°. There is a single inlet injector on one of the 9° ramps, positioned 80 mm horizontally upstream of the throat on the engine center line at a 45° angle to the local flow. Differently from the experimental model, which is 75-mm wide from the start of the 9° ramps, where the sidewalls start, the computational grid is 64-mm wide. This is due to a change in the experimental model, which was made wider to fit available mounting structures to the test section. The engine was developed with enough width at 64 mm that the fuel plume does not interact with the walls, meaning that the fuel plume and reaction region are equivalent for both the 64 mm and 75 mm cases. The 6° forebody remains wider, to avoid edge effects from being ingested by the engine, and has no sidewalls. The boundary-layer trips used in the experiments were not included in the simulations. This is because it was originally intended for the experiments to be performed without trips, relying on the fuel injection process to trip the flow. This will be shown to be adequate in the simulations, which feature a steady inflow. As previously mentioned, the trips were found to be necessary to maintain properly started flow throughout the engine during the impulsive experiments. Given the complex geometry of the trips, their flow structures could not have been resolved here without considerable computational cost. Considering the lack of trips shows little impact on the capability of the LES to capture the overall flow structures, as will be discussed in Section III, it was instead opted to not account for their effect on the flow through direct modelling.

The simulation was completed in two parts. First, an unfuelled laminar simulation of the intake up to the throat is performed to convergence. The results from this simulation are then used as the input for the LES by using a subroutine to interpolate the cell values from the laminar grid [44]. This is shown in Fig. 5, with indication of the regions where laminar and LES solutions were obtained. The LES grid starts just downstream from the ramp corners, upstream of the injector, with turbulent viscosity production enabled by introducing a very low level of free-stream turbulent viscosity. This process has two main advantages. First, it reduces the size of the LES grid, saving on computational time. Second, it forces transition to happen closer to the region where boundary-layer trips were used in the experiment,

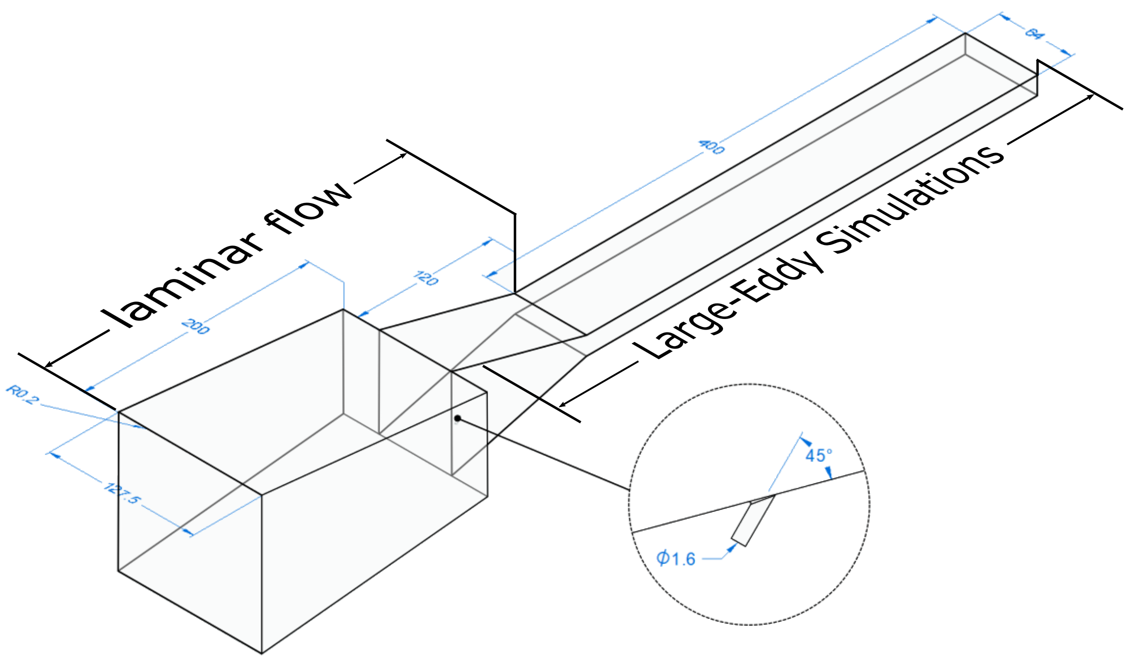

Fig. 5 Full computational domain used in the simulations of the experimental model. Regions where either laminar or Large-Eddy simulations were performed are indicated. Dimensions are in mm.

Table 2 Nominal conditions used as inflow for the LES simulations.

		Free-stream	Injector
ρ_∞	[kg/m^3]	0.025	1.07
T_∞	[K]	407	249
u_∞	[m/s]	2972	1203
Y_{N_2}	-	0.7312	-
Y_{O_2}	-	0.1908	-
Y_{NO}	-	0.0769	-
Y_O	-	0.0011	-
Y_{H_2}	-	-	1.0
$\dot{m}_{H_2}$	[kg/m^3]	-	2.7×10^{-3}

more accurately capturing the physics of the experiment than either purely laminar or turbulent flow would achieve. This compensates somewhat for the lack of boundary-layer trips in the simulations. To reduce computational cost even further, the nozzle was not included in the simulations. The resulting LES grid has approximately 69 million cells.

To verify the quality of the grid, the turbulent kinetic energy is analysed to determine how much of it is resolved. Ideally, 80% of the turbulent kinetic energy should be resolved in a well-resolved LES [45]. This can be determined by:

$$R = \frac{k_r}{k_r + k_{sgs}}, \tag{15}$$

where k_r and k_{sgs} are, respectively, the resolved and modelled turbulent kinetic energy. Fig. 6 shows this parameter R

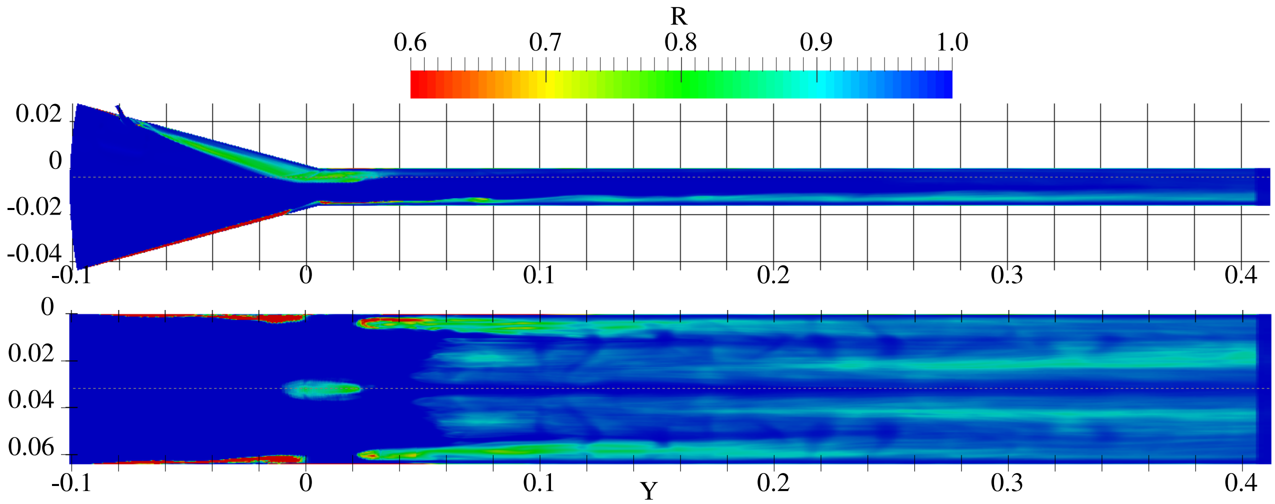

Fig. 6 Proportion of turbulent kinetic energy that is resolved on the center-plane (top) and bottom wall (bottom) of the grid.

on the center-plane of the model. As can be seen, most of the turbulent kinetic energy is resolved sufficiently, with $R \geq 0.8$. The only exception is close to the wall on the ramp opposite the injector, and upstream of the injector. This is not a problem, however, as wall regions are intentionally spatially under-resolved as part of the IDDES approach (see Section II.B). The lower value of R in these regions is, therefore, expected.

The inflow conditions for the simulations, shown in Table 2, are meant to reproduce the experimental conditions shown in Table 1. The velocity inflow boundary condition in US3D uses flow density, temperature and velocity to determine the overall inflow. This boundary condition is used for both the free-stream and fuel injector. As shown in Fig. 5, the injector inflow is prescribed upstream of the injector exit into the flow, on the duct. The injector inflow was determined to produce a fuel equivalence ratio $\phi = 0.15$. The values used for both free-stream and injector are shown in Table 2. Since the objective is to reproduce the experiments, not flight conditions, the simulations also include NO and O species in the free-stream.

III. Experimental results

A. Wall pressure data analysis

The analysis begins with normalised wall pressure data obtained during the experiments, shown in Fig. 7, which presents the averaged pressure values for the unfuelled shot (12087), $\phi = 0.18$ (shots 12088 to 12090) and $\phi = 0.13$ (shots 12092, 12094 and 12095). The error bars are the standard deviation for all the shots considered, except for the unfuelled case where the experimental uncertainty was used. Results for LES and for an unfuelled RANS case are included for comparison. The shots using the injector-only (IO) configuration were not included as pressure data was not obtained for the entire engine as only the bottom half of the engine was used for optical access to the injector region (see

Table 3   Summary of the shots analysed.

Shot number	Engine configuration	Equivalence ratio
12087	combustor front (CF)	-
12089	CF	0.17
12090	CF	0.18
12092 to 12095	CF	0.13[a]
12096	combustor rear (CR)	0.13
12097	CR	0.12
12098	CR	0.13
12100 to 12104	injector only (IO)	0.13
12111	IO	0.15

[a] Plenum pressure failed to record for shot 12093. Since Ludwieg tube pressure was recorded and consistent with other shots, the equivalence ratio was assumed to have been the same.

Section II.A). Table 3 contains information regarding the experimental tests (shots) used in this work for quick reference.

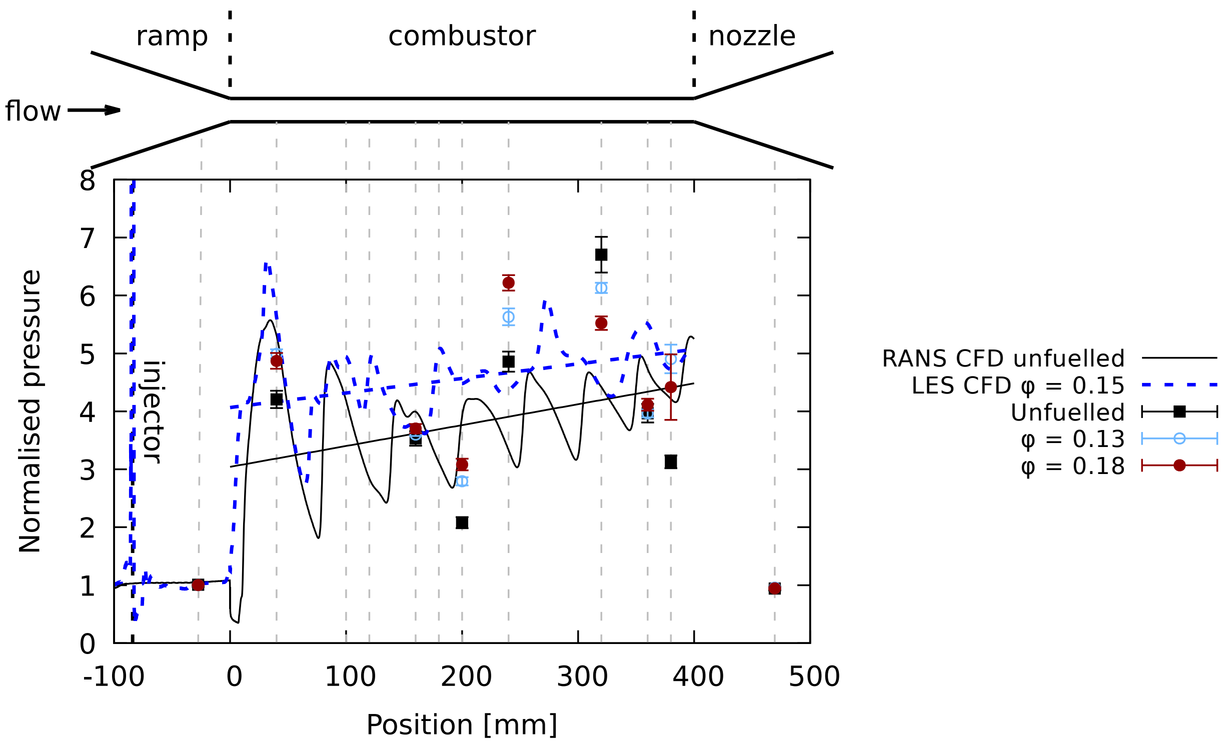

Fig. 7   Averaged normalised wall pressure data for the experiments separated by fuel equivalence ratio, and numerical simulations. The straight lines are a linear curve fit of the numerical pressure values inside the combustor.

Several observations can be made from these pressure results. First of all, agreement with CFD is generally good, with LES presenting overall better agreement than RANS. There is a small pressure offset in the combustor between fuelled and unfuelled shots. This is due to extra compression obtained by the injected mass. There is little observable pressure rise from combustion. Combustion does take place, as will be shown in the OH-PLIF results later, but since the fuelling rate is so low (much lower than what would be used in a real scramjet), the combustion-induced pressure rise is small. Comparing the fuelled shots against the unfuelled one, it can be seen that the peaks and troughs move, which indicates the shock train being displaced by fuelling. For the first half of the combustor, it can be seen that the unfuelled shot has the lowest pressure. Fuelled shots have higher pressure, with the pressure offset increasing with fuel equivalence ratio. This changes in the last quarter of the combustor, past $x = 300$ mm. At $x = 320$ mm the pressure values are reversed, with the unfuelled case presenting the highest pressure. This is most likely due to displacement of the shock structures caused by fuel injection. The presence of the shock structure is clear in the numerical results.

In terms of the numerical results, it can be seen that the unfuelled RANS results produce a regular shock-train structure with well-defined peaks and troughs. The fuelled LES, on the other hand, does not have a well-defined shock train. Peaks and troughs are visible, but their structure is irregular. There is also a clear pressure offset between the RANS and LES results, due to fuel injection and possibly combustion in the LES case. This is clearly seen in the straight lines in Fig. 7, which are linear curve fits of the pressure results inside the combustor for both CFD cases. The experimental results seem to indicate there is a single wavelength along the combustor, with peaks at around 50 and 300 mm, which is not captured by the simulations, even though there is good overall agreement between simulations and experiment in the average values. This could be because the gaps in the pressure sensor coverage conceal further variation in the pressure traces inside the engine. Another important factor in the distinction between experiments and simulations may be due to the use of boundary-layer trips, as will be discussed in detail in Section IV. The boundary-layer trips introduce considerable non-uniformities to the flow, as shown in Fig. 12. These include extra shock waves nearly as strong as those produced by the intake ramps. These extra flow futures can and certainly do alter the flow field inside the combustor, which would not be captured by the simulations as they lack the boundary-layer trips.

Figure 7 also highlights the repeatability of the experiments, with the small standard deviation showing small shot-to-shot variation. While these results are useful for verifying the behavior of the engine at different conditions and for a quick comparison with CFD. The pressure measurements by themselves do not, however, provide much information on the combustion process. This is discussed in the next section.

B. Flame visualisation

As discussed in Section II, OH-PLIF diagnostics have been used for experimental flame visualisation at different locations of the engine. These results are shown in this section and later, in Section IV, they are compared with snapshots of the LES simulations for a geometry and conditions representative of the experiments. Before discussing these results, however, a comment must be made on the images obtained at the end of the combustor. As discussed earlier, to obtain these images the model had to be moved so that the laser could be projected into the region of interest. This is due to limited optical access in the test section. Because of this, the model intake area seems to have moved partially outside the nozzle core-flow, resulting in less mass flow rate at the edges, which impacted the wall pressure results in the second half of the combustor. This might impact combustion at this region, mostly likely by reducing the rate of combustion due to lower pressure and mass flow rate caused by the non-uniform inflow. However, since the pressures agree for half of the combustor, and ignition happens early in the combustor, as will be shown in this section, the obtained OH-PLIF results are likely to be still representative of the entire combustion process. As will be seen, there is a clear progression in the height of the combustor occupied by OH radicals, indicating an increase in the reaction zone. This also agrees with the simulations. Therefore, the following results are believed to paint a complete picture of the combustion process in a scramjet engine. The reduced capture affecting wall pressure data of the rear of the combustor is expected to only have a weak effect on flame structures and combustion regimes.

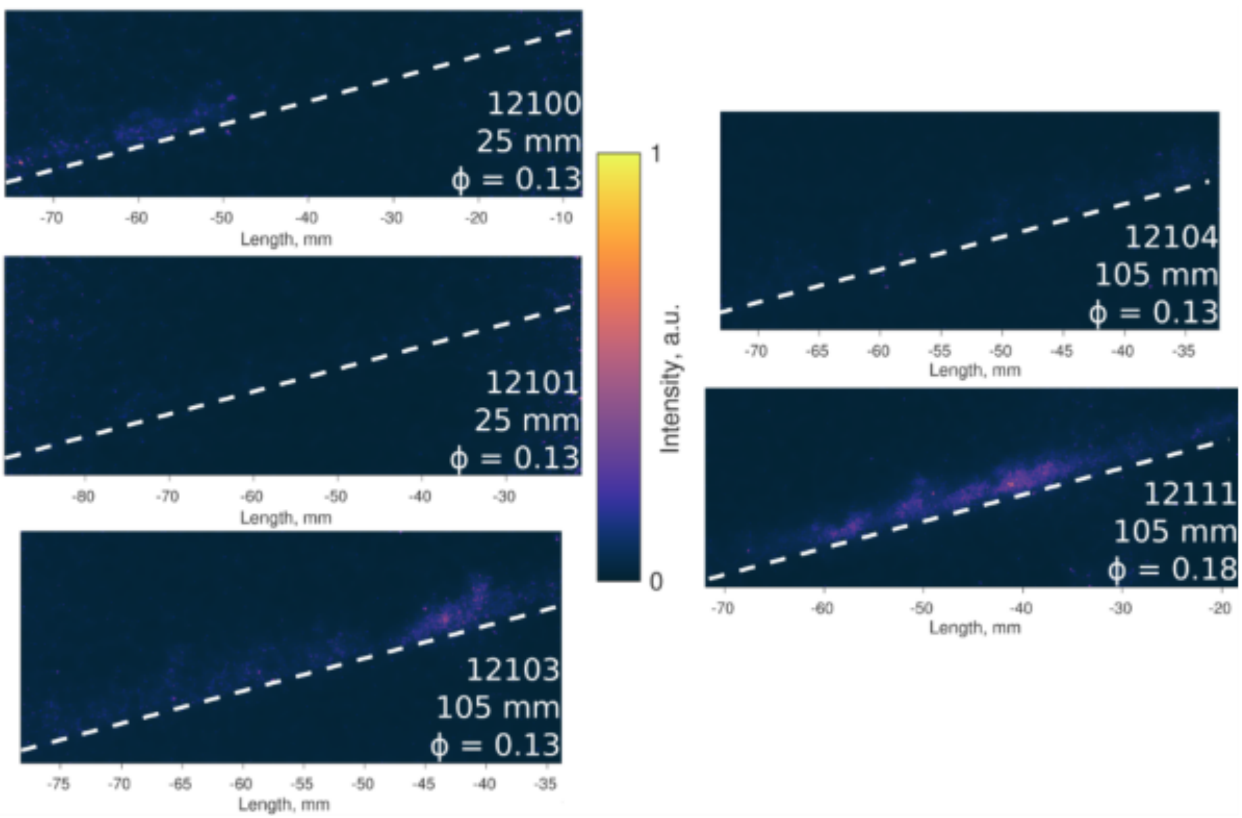

Fig. 8 OH-PLIF results for the injector region obtained with the injector-only configuration. The dashed line indicates the position of the 15° **ramp. The text indicates, from top to bottom: shot number, lens focal length and equivalence ratio.**

Figures 8, 9, and 10 show the experimental OH-PLIF results obtained for the injector only (IO), combustor front (CF) and combustor rear (CR) configurations, respectively. These images represent an instantaneous snapshot of the transient flow state at time $t = 2$ ms, which is within the steady test time for the shots (see Section II.A). The images were obtained either with a 25-mm or 105-mm focal length lens, indicated accordingly. The position in the horizontal axis indicates the horizontal position along the engine, with $x = 0$ being the location of the throat, i.e. the start of the combustor (see Fig. 1).

We begin the analysis with the images obtained in the compression ramp, downstream of the injector, shown in Fig. 8. Even though this region is just downstream of the injector (located at $x = -80$ mm) and the flow hasn't been fully processed by the intake shocks, chemical activity can be observed. The signal is weak, an indication that chemical reactions are not intense and there is limited OH production in this region. In fact, on shot 12101, if any OH is present, it is indistinguishable from the background noise. These results indicate reactions start early in the engine even before interaction with shocks. This is mostly likely due to the bow shock, behind which conditions are suitable for quick ignition as soon as fuel and air mix [46]. The overall behavior seems to be of a thin layer of OH close to the wall, with a thickness of about 5 mm. It can also be seen that the shot with higher equivalence ratio, shot 12111, presents a much

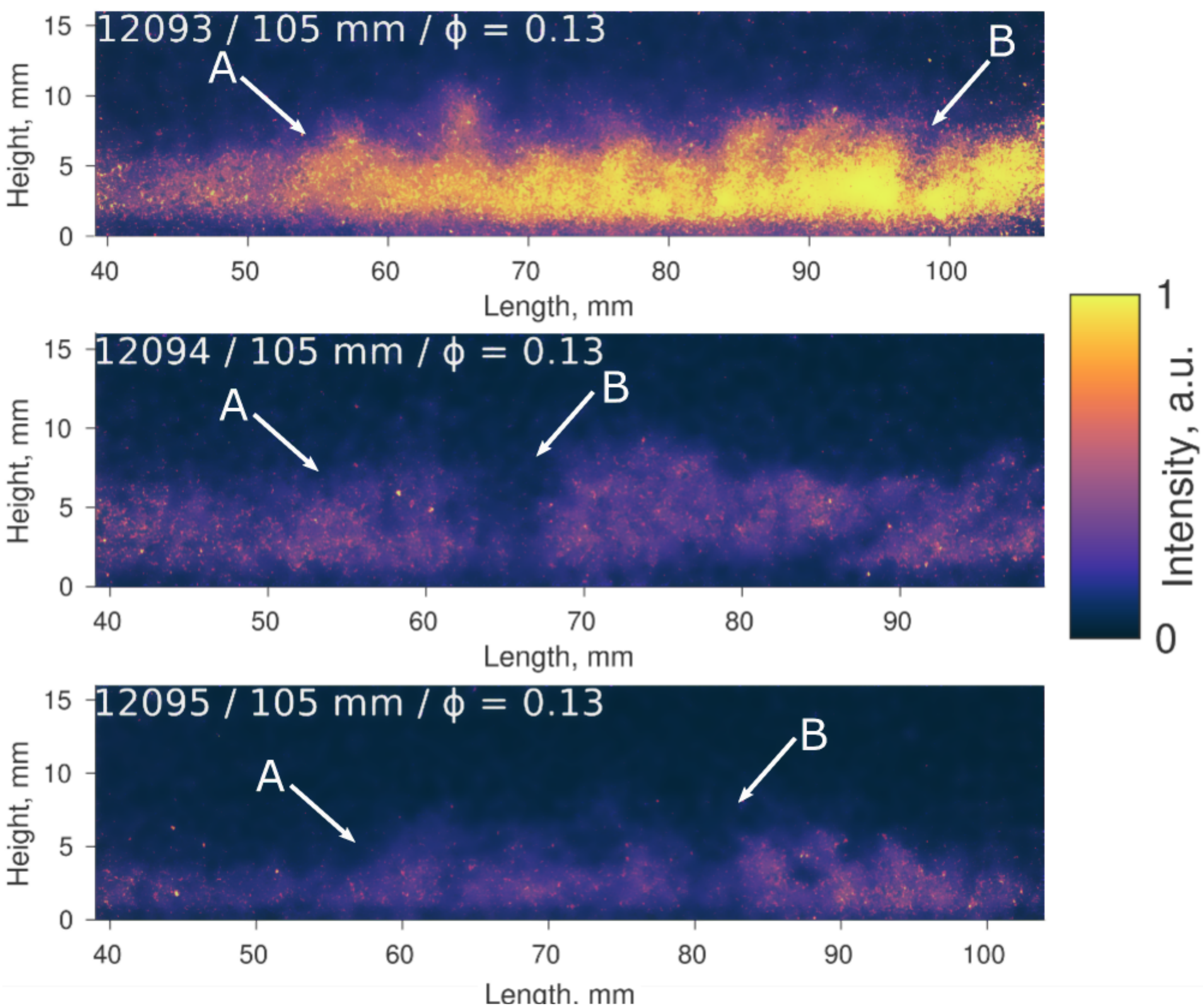

Fig. 9 OH-PLIF results for the first third of the combustor, obtained with the combustor-front configuration. The text indicates, from left to right: shot number, lens focal length and equivalence ratio. Notes A and B respectively indicate large turbulent structures and "valleys" where there seem to be gaps in the OH distribution, respectively.

stronger signal, indicating even a small increase in equivalence ratio is enough to enhance chemical activity in this region [47]. Large turbulent structures can be seen, particularly in shots 12103 and 12111. Resolution is not high enough to discern smaller structures.

It is unknown why shot 12100 behaves as it does, with a short region of OH followed by no signal. Collisional quenching of the fluorescence signal, which is more prominent with higher pressures, is unlikely here as the pressure in this region is expected to be low. The region is within the laser sheet. It is possible that there is a burst of OH production in the injector bow shock, which is then consumed before conditions are appropriate to generate more OH radicals. It could also be the result of unsteadiness of the flow as the PLIF image is not time-averaged, or the OH could be moving out of the plane of the laser sheet.

Moving into the combustor, Fig. 9 shows the OH-PLIF images obtained at the start of the combustor, about 40 mm downstream of the throat and up to around 100 mm into the combustor. In this region, the flow has been fully processed by the intake shocks. The signal is much stronger in this region. The OH is now distributed in a thicker zone, occupying about half the combustor height, around 7.5-mm thick. At certain locations it reaches a thickness close to 10 mm. Turbulent structures are more discernible in these images, with large vortical structures present on the interface between the OH and the air without fuel above it. The signal intensity is similar between shots, indicating a similar combustion level between them. The exception is shot 12093, which clearly presents a much stronger signal. There was no change in the measured tunnel conditions and wall pressure in the model for this shot. The fuel plenum pressure failed to record

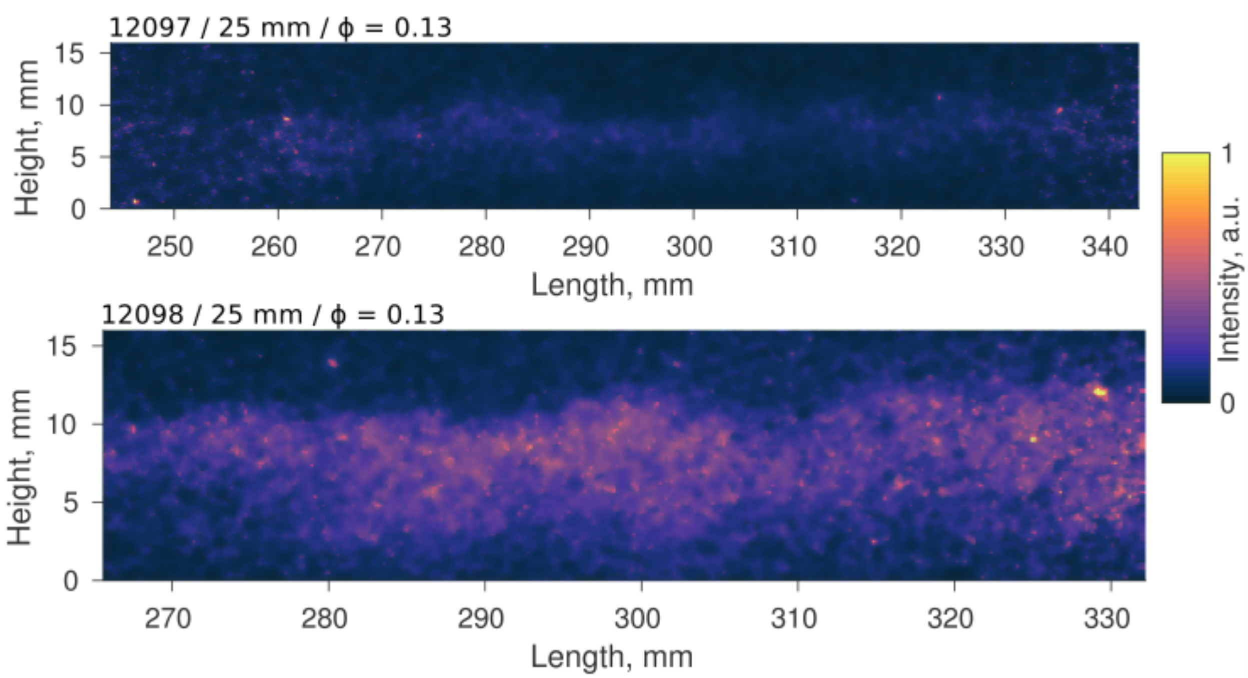

Fig. 10 OH-PLIF results for the latter third of the combustor, obtained with the combustor-rear configuration. The text indicates, from left to right: shot number, lens focal length and equivalence ratio.

for this shot and the equivalence ratio is not known. However, the Ludwieg tube pressure was recorded and was on the same level as the shots that consistently produced an equivalence ratio $\phi = 0.13$, so it is reasonable to assume the equivalence ratio for this shot was the same. Therefore, the higher intensity cannot be easily attributed to anything other than unsteadiness in the flow. Regardless of the signal intensity, the structures that can be observed are quite similar between the shots. There seems to be a less turbulent region up to around 50 mm, where large turbulent structures become visible (note A). These turbulent structures distort the boundary between the OH and the unfuelled air, which is the boundary of the flame, making it more wrinkled and convoluted. In all three shots there are regions where "valleys" can be seen (note B), where the flame boundary moves towards the bottom wall by a substantial distance.

Finally, Fig. 10 shows the PLIF images obtained at the end of the combustor, between around 250 and 340 mm. Even though this is the end of the combustor, the signal remains weak due to the small quantity of fuel being injected, which means OH concentrations are low throughout the engine. It can be seen that the region occupied by OH increases further, almost reaching the top wall of the combustor, indicating the progress of combustion, leading to more OH being generated. Unlike the images from the start of the combustor, the flame boundary is less convoluted, and no large turbulent structures can be discerned on the flame. From the OH-PLIF images alone it is hard to determine the cause, but it can be inferred. At this stage the combustion process should be stronger and the rate of heat release higher. This leads to faster chemistry, which could lead to a flame that is less affected by turbulence, causing the smoother flame boundary seen in these images. Another important observation in these images is that the signal is weaker close to the lower wall. This could indicate the OH has been consumed in this region and combustion is closer to completion, as would be expected at the end of the combustor.

These results provide great insight into the combustion process. Chemical activity happens early, near the injector, and combustion seems to happen in thick regions in the fuel plume. These regions increase in thickness as the flow moves through the engine, indicating more mixing and combustion. The flame is initially clearly affected by turbulence, presenting a convoluted flame boundary where large turbulent structures can be seen. This changes towards the end of the combustor, where the flame boundary is smoother, and the turbulent structures are not discernible, most likely a result of faster chemistry at this point in the combustion process, when completion rate is higher. This behavior is quite different from the one observed by [17], as the flow in the engine is highly non-uniform and provides better mixing, leading to different flame structures. This will be analysed in more detail in the next section.

IV. Numerical results

In this section, the Large-Eddy Simulations results are analysed. The numerical results are first compared with the experiments to verify if LES is capable of accurately simulating the experimental conditions. The presented data from the LES are instantaneous snapshots of the transient simulations. Replicating the precise time history of the experimental flow is, of course, impossible, but the simulations aim to represent a field that is statistically equivalent.

The simulations are run for at least three flow lengths (≈ 1ms), i.e. enough time for the flow to pass through the model three times. This is the same criterion used in the experiments to determine a test time over which the flow is steady, as discussed in Section II.A. Figure 11 shows the LES results for OH density at slices located at the center plane ($z = 0$) and offset from the center plane at $z = +1$, $+2$ and $+3$ mm.

Fig. 11 OH density for stream-wise slices. From top to bottom, respectively: center plane ($z = 0$), $z = +1$ mm, $z = +2$ mm and $z = +3$ mm.

As has been discussed in Section II.B.2, the simulation was done in two parts, with the LES solutions starting from the second set of ramps. Therefore, the LES results start at the 15° ramps. As can be seen, the center plane in the simulations does not resemble the PLIF images, which were set up to be taken at the supposed model center plane. Only by moving off-center by a couple of millimetres does the LES visually approach the experimental results. There are two main reasons for this. The first one is the lack of boundary-layer trips. As has been stated previously, the LES simulations do not include the boundary-layer trip in the intake, which generates a more turbulent flow-field than what would be obtained with only the fuel injection to promote transition. The typical shock structures around injectors [48] have little gradient in the span-wise direction and thus do not amplify fluctuations, particularly in the center plane where the counter-rotating vortex pair does not meet, which leads to a less turbulent flow in the region. In contrast, let us investigate the shock structure generated by the trips. Figure 12 shows schlieren imaging from shot 12086, taken at the forebody where the trips are located. The shock structure produced by the trip can be clearly seen. There is a detached shock generated by the trip, with a weaker secondary shock generated in the spaces between the teeth on the trip. The blunt trip profile creates a separation region upstream of it, which generates a separation shock, as well as a smaller separation downstream from the trip. This structure is very complex [49]. The separation regions and shocks on the teeth of the trip should create a very three-dimensional flow-field. It is known that boundary-layer trips increase turbulence in the flow, moving transition onset upstream, even in high Mach number flows such as the one analysed here [49, 50]. Therefore the trips in the experiment present a much more complicated shock structure which varies span-wise, due to the teeth distribution, compared to the shock structured around the injector. This would increase non-uniformities and mixing in the span-wise direction. The flow-field in the simulation, therefore, should have slower mixing than the experimental flow-field, which means it takes longer to generate the thicker OH zones seen in the experiment. The slices at z = +2 and +3 mm show this, with the progression in the thickness of the OH region being similar to that observed in the experiment, albeit starting at a location further downstream in the simulations.

The trip used in the experiment is therefore the likely cause for the discrepancies between experimental PLIF and LES results on the center plane. The increased turbulence and the separations around the trip create a turbulent, three-dimensional flow that increases overall mixing, including in the span-wise direction. Therefore, the flow seen in the center-plane of the simulations would be perturbed and the clear separation between each vortex in the CVP would probably disappear. This is the most likely cause for the discrepancies between simulations and experiment.

The second possible reason for the difference seen in the center plane between experiment and simulations is uncertainty in position of the laser sheet in the experiment. The laser was aligned into the engine using millimetre graph paper, which is done at the lowest possible power setting for safety reasons. This makes detection of the sheet more difficult, which creates some uncertainty as to its accurate position. This could potentially lead to an uncertainty of one or two millimetres. The width of the laser sheet, and therefore spatial integration, is an unlikely cause as the focusing optics are configured to provide a very thin sheet. The position of the model is also unlikely an issue as the tolerances in model position and the internal flow-path were all strictly designed, with no tolerances higher than 0.1 mm.

Figure 13 shows the stream-wise plane at z = +3 mm for numerical OH species density, along with shots 12094, 12098 and 12103 in their correct position along the engine. The dotted lines point to a region in the LES flow that is similar to the OH-PLIF image for shot 12094, taken at the start of the combustor. Both can be seen in the detail in the figure. As can be seen, the region at the start of the combustor in the experiments is similar to regions much further downstream in the LES, towards the end of the combustor. This is a further indication that the mixing in the simulations is slower than the experimental engine due to the lack of the boundary-layer trips. Even with the apparent limitations of the simulation in directly reproducing this specific experiment, the LES results can capture the overall behavior of the

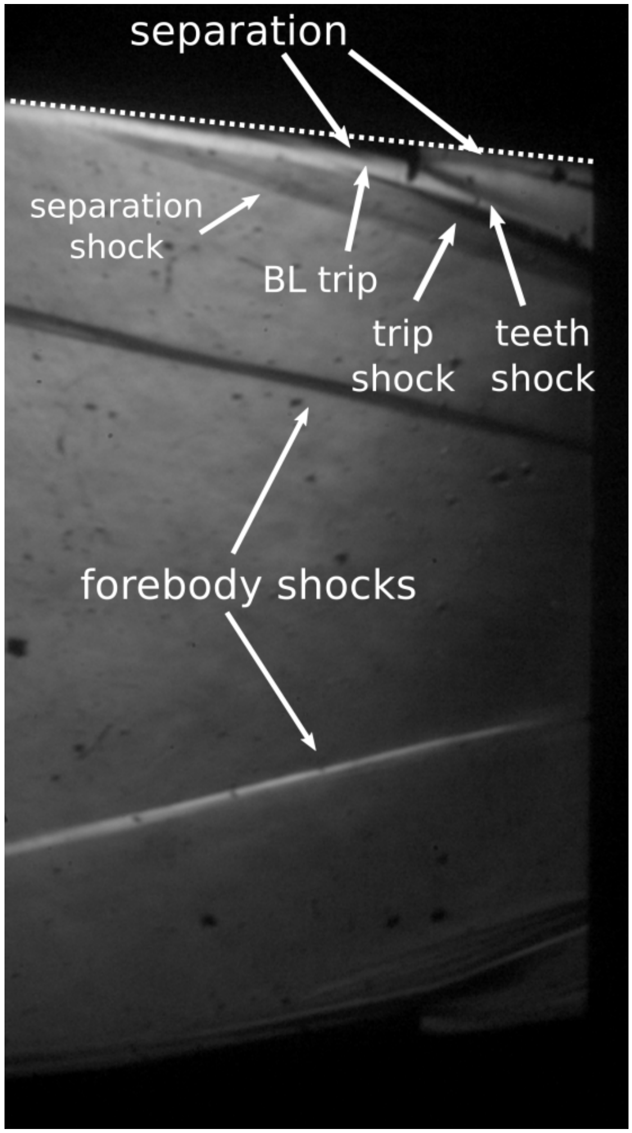

Fig. 12 Schlieren imaging of the forebody with boundary-layer trips for shot 12086. The dotted line indicates the position of the forebody ramp. Since the structure is the same on both ramps, details are given only for the top ramp.

engine flow and, more importantly, of the combustion process.

Since the stream-wise plane at $z = +3$ mm is more representative of the experiments, due to the reasons discussed in the preceding paragraphs, that plane is used for the results in the following section, where the simulation results are analysed in more detail for better insight into the flow features and combustor state.

A. Flow field and flow properties

Figure 14 shows OH and H_2O mass fractions, and enthalpy of formation for the mixture. The enthalpy of formation represents heat release and has negative values as the process is exothermic. The contours are shown at several span-wise slices along the engine, as well as in the stream-wise plane at $z = +3$ mm. The images show that most of the chemical activity happens around the counter-rotating vortex pair created by the fuel injection and bow shock. The CVP itself is quite symmetric, likely due to the lack of boundary layer trips, and it moves unmixed oxidiser into the reaction zones. As a result, OH and H_2O production are highest along its boundary and the heat release distribution reflects this. Interestingly, in these simulations it can be seen that the length of the combustor is not enough for the CVP to meet at the combustor center, where chemical activity is constrained to a very thin region close to the wall.

The simulations indicate that OH is indeed present just downstream of the injector, although its behavior is different from the experiment. Here, it is present at the edge of the fuel plume, following the bow shock, and not in a thicker turbulent zone close to the wall. This could be due to lower mixing and lack of resolved turbulence originating from the boundary-layer trip, or even the lack of resolved turbulence close to the wall downstream of the injector, as the region is modelled in the IDDES approach used in this work. The definite cause of the difference is uncertain. Regardless, it agrees with experiment in that chemical activity is present as far upstream as fuel is introduced and in fact simulations

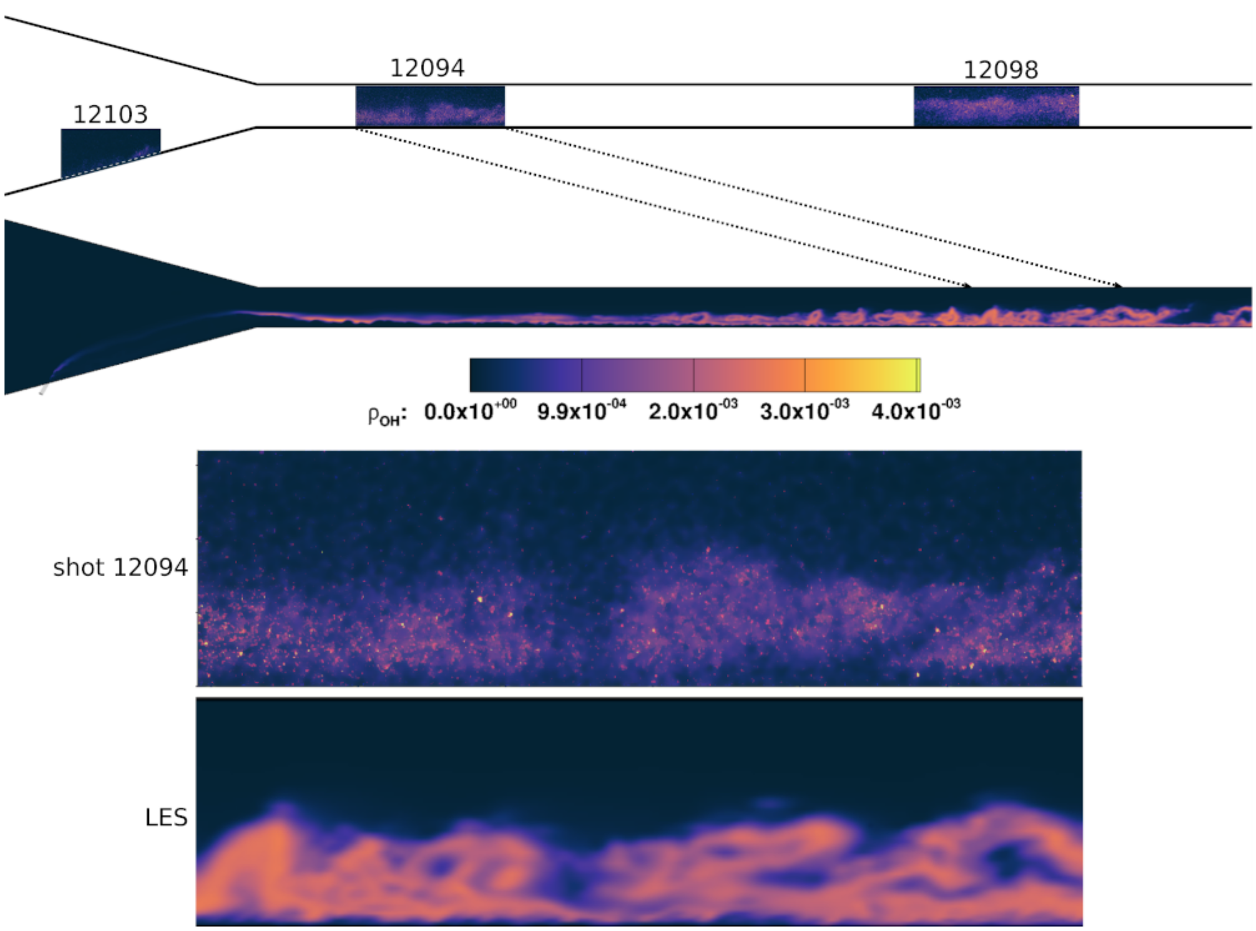

Fig. 13 Comparison between experimental OH-PLIF results for shots 12094, 12098 and 12103 and the numerical OH species density at the stream-wise plane at $z = +3$ mm. The PLIF image for shot 12094 on the bottom was denoised with a selective Gaussian filter.

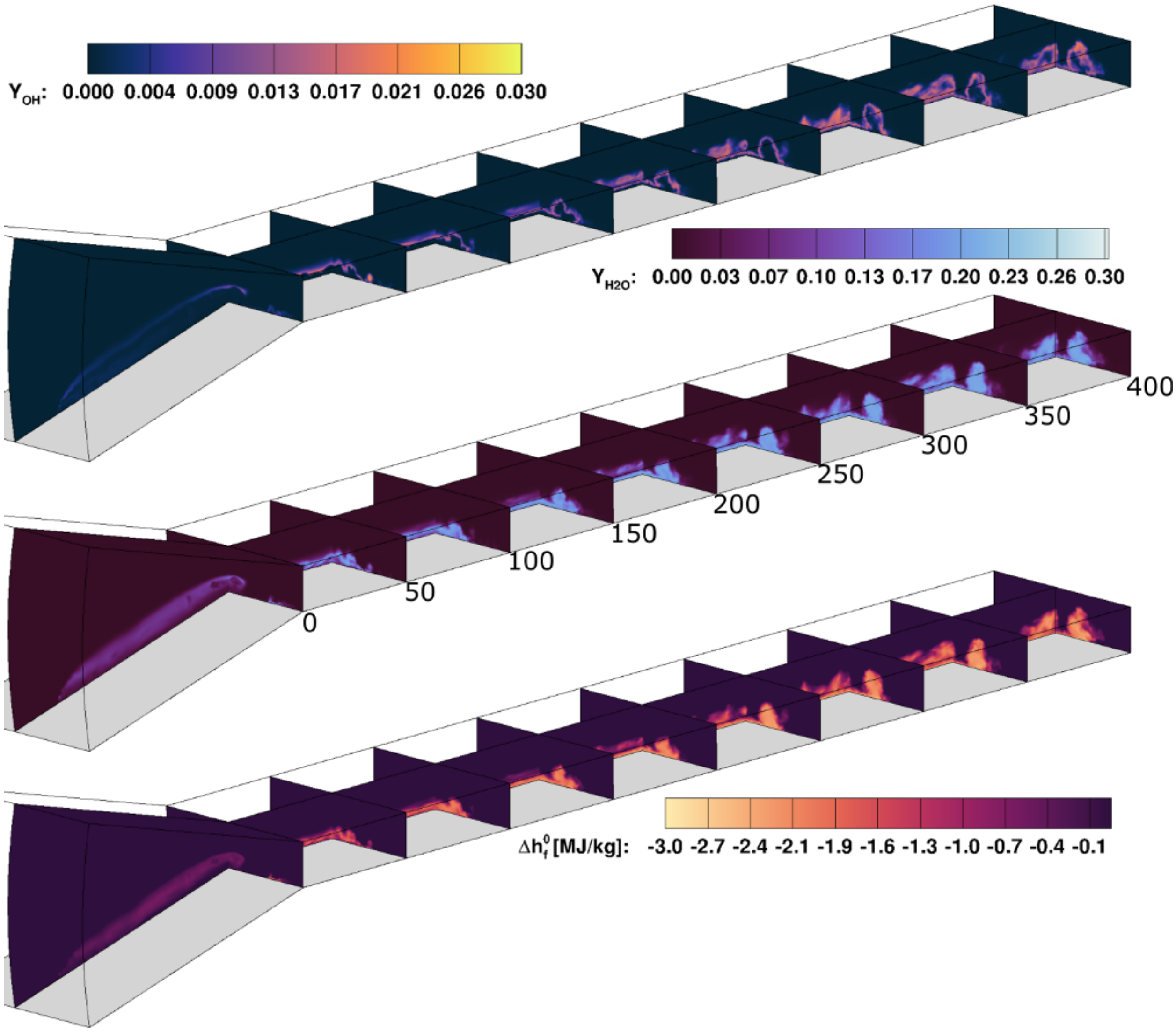

Fig. 14 From top to bottom: contours of OH mass fraction, H_2O mass fraction and enthalpy of formation for $\phi = 0.15$ (stream-wise plane at $z = +3$). Inflow conditions in Table 2.

indicate combustion reactions are completed in this region, generating H_2O and promoting heat release upstream of the throat, albeit at low levels. It has been previously observed that the bow shock in a porthole injector is capable of producing sufficient conditions for hydrogen autoignition [46]. It is also evident from the experiments there is a considerable increase in chemical activity as the flow enters the combustor, where it is fully processed by the intake shocks, leading to higher radical production and heat release.

Figure 15 shows contours for pressure, temperature and Mach number. For temperature and Mach number, it can be seen that the effects of combustion are localised around the fuel plume. The flow gets hotter around the CVP, where heat release is most intense. As a consequence of the temperature increase, Mach number is reduced in the same region. The

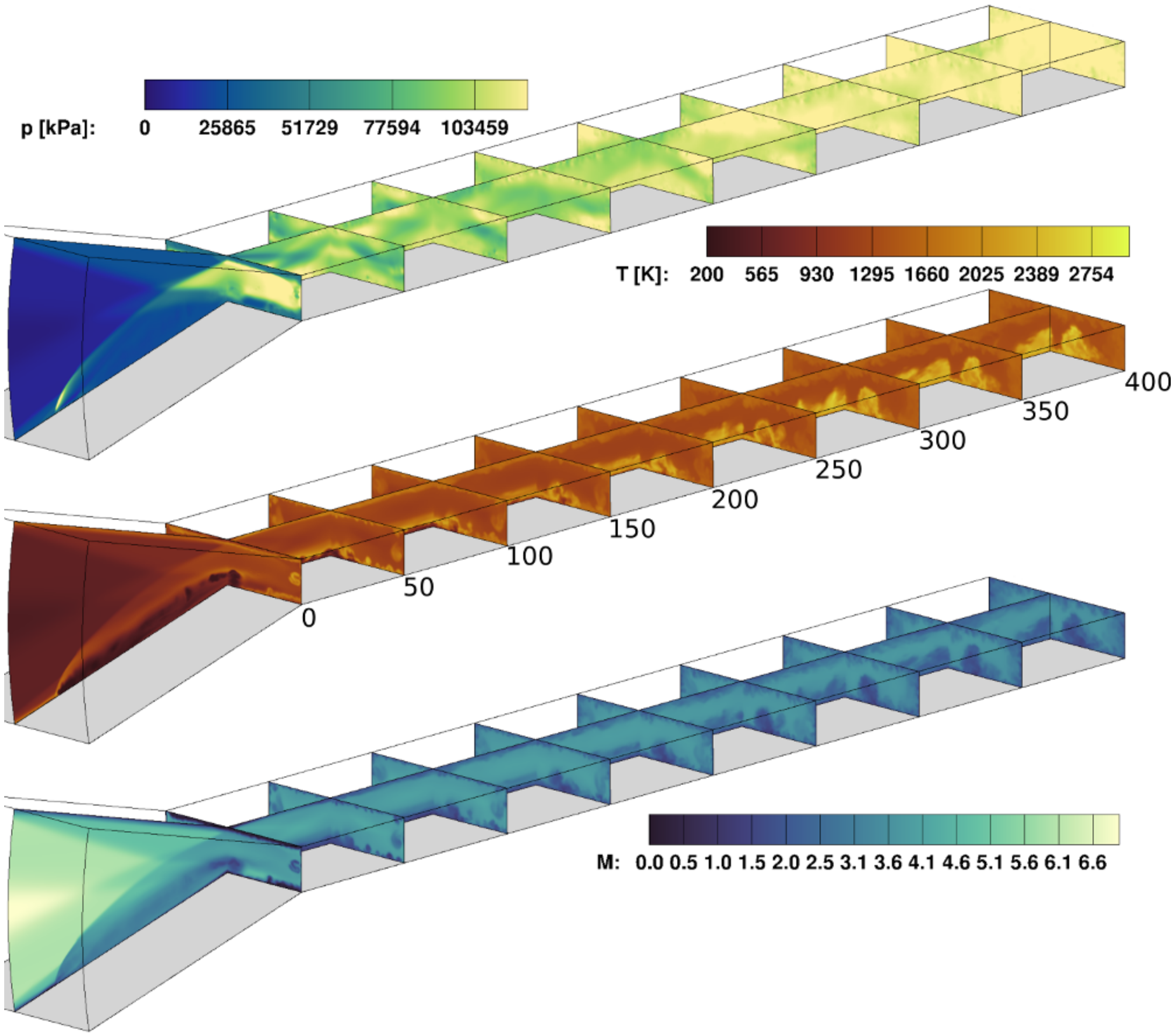

Fig. 15 From top to bottom: contours of pressure, temperature and Mach number for $\phi = 0.15$ (stream-wise plane at $z = +3$). Inflow conditions in Table 2.

fuel plume quickly heats up as well, with the cold regions remaining close to the wall up to 100 mm into the combustor. It can be clearly seen that the core of the CVP remains at a colder temperature than its edges, as the CVP keep mixed fuel away from their cores.

As for pressure, it can be seen that there is a constant increase in pressure levels as the flow moves down the combustor. The reflected shocks from the intake hit the combustor close to the throat, meaning the flow is fully processed by the intake shocks right from the start of the combustor. The shock train thus formed is visible up to about half the combustor length, where it gets dissipated by turbulence. This was also shown in Fig. 7, where in the fuelled LES results the shock train is irregular and disappears towards the end of the combustor.

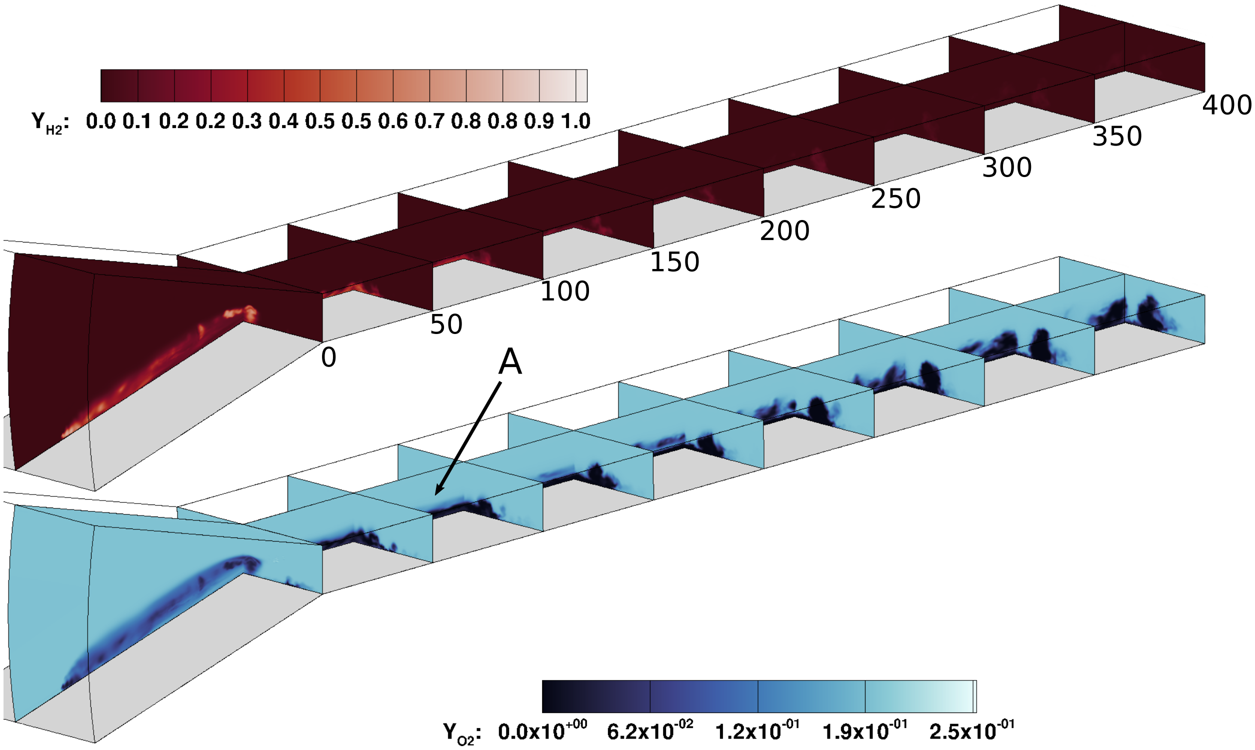

Fig. 16 Contours of H_2 mass fraction (top) and O_2 mass fraction (bottom) for $\phi = 0.15$ (stream-wise plane at $z = +3$).

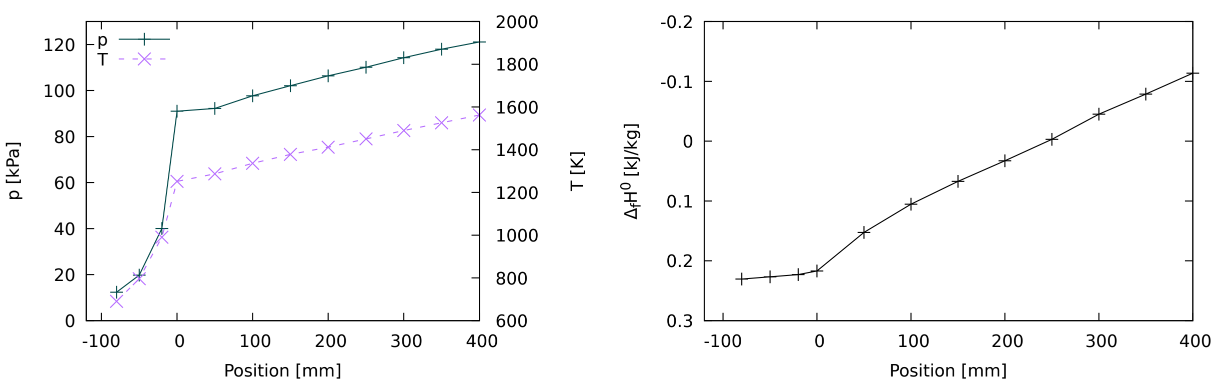

(a) **(b)**

Fig. 17 (a) Averaged pressure and mass-flow-rate averaged temperature, and (b) mass-flow-rate averaged enthalpy of formation of all species, across span-wise slices along the engine for $\phi = 0.15$. Please note the y-axis for enthalpy of formation is inverted as negative enthalpy of formation corresponds to an exothermic process.

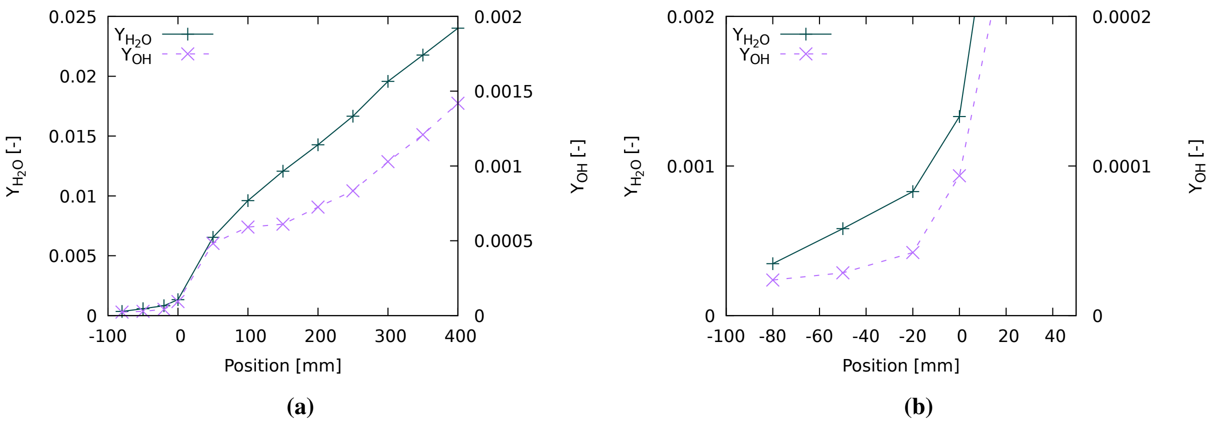

Fig. 18 (a) Mass-flow-rate averaged OH and H_2O mass fractions with (b) a detail of the ramp region, across span-wise slices along the engine for $\phi = 0.15$.

Figure 17 and 18 show the averaged pressure and mass-flow-rate-weighted averaged temperature, OH and H_2O mass fractions, and enthalpy of formation of all species in the gas mixture at different axial locations in the simulation. It can be seen the flow is quickly compressed as it goes through the throat, as was discussed previously. Pressure and temperature both increase quickly up to the throat, after which there is a more modest rate of increase for both pressure and temperature. Pressure and temperature at the throat reach approximately 60 kPa and 1200 K, values above autoignition conditions for hydrogen. This corroborates the discussion above, as these conditions, for a flow seeded with radicals, would quickly intensify the combustion rate. This is seen in Fig. 18a, where there is a considerable increase in the mass fraction of OH and H_2O at the start of the combustor, up to around $x = 50$ mm. Both species are already present in small quantities upstream of the injector, as seen in the contours in Fig. 14. After this point, water increases at a steady, albeit slightly slower, rate. For OH, however, the increase rate drops sharply between $x = 50$ and 250 mm, after which it recovers and increases at the same rate as H_2O. This indicates OH is consumed faster than it is produced in the first half of the combustor, which indicates mixing-limited combustion as has been identified earlier. Finally, it can be seen in Fig. 17b that the enthalpy of formation of all species in the mixture, which represents heat release, increases quickly into the combustor, as expected from the results discussed above. The rate of increase for enthalpy of formation follows that of water, which is the species whose production most contributes to heat release.

B. Mixing and combustion efficiency

In this section, the mixing and combustion efficiencies are presented for the engine. The mixing efficiency is defined as [51]

$$\eta_{\mathrm{m}} = \oint \int Y_{\mathrm{H}_2} \rho u \,\mathrm{d}y\mathrm{d}z \Bigg/ \oint \int Y^{\mathrm{r}}_{\mathrm{H}_2} \rho u \,\mathrm{d}y\mathrm{d}z, \tag{16}$$

where

$$Y^{\mathrm{r}}_{\mathrm{H_2}} = \begin{cases} Y_{\mathrm{H_2}} & Y_{\mathrm{H_2}} \leq Y^{\mathrm{stoic}}_{\mathrm{H_2}} \\ \left(\frac{1-Y_{\mathrm{H_2}}}{1-Y^{\mathrm{stoic}}_{\mathrm{H_2}}}\right) Y^{\mathrm{stoic}}_{\mathrm{H_2}} & Y_{\mathrm{H_2}} > Y^{\mathrm{stoic}}_{\mathrm{H_2}} \end{cases}. \tag{17}$$

The term $Y^{\mathrm{stoic}}_{\mathrm{H_2}}$ is the stoichiometric mass fraction for a hydrogen-air mixture. Combustion efficiency represents how much of the hydrogen mass available has been converted into water [52] and is defined as

$$\eta_{\mathrm{c}} = \frac{0.1119\, \dot{m}_{\mathrm{H_2O}}}{\dot{m}_{\mathrm{H_2,injected}}}. \tag{18}$$

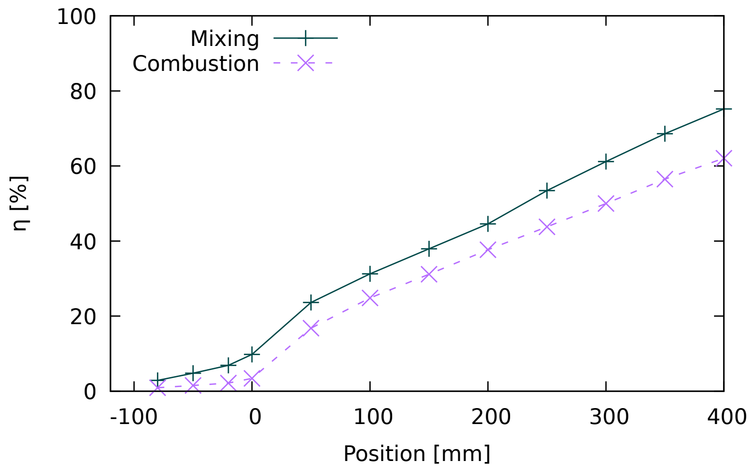

Fig. 19 Mixing and combustion efficiencies across span-wise slices along the engine for $\phi = 0.15$.

Figure 19 shows mixing and combustion efficiencies at span-wise slices along the engine. There is a fast increase in both mixing and combustion efficiency as the flow enters the combustor, coinciding with the observed increase in OH and H_2O mass fractions in Fig. 18a. This sudden increase in mixing rate is due to the strong vorticity generated in the inlet shock-fuel plume interaction [53]. The rate is initially higher for both efficiencies, up to around $x = 50$ mm, reducing downstream. For the remainder of the combustor, the rate of increase for both efficiencies is very similar, with mixing efficiency increasing slightly faster, particularly after $x = 250$ mm. This is another indication of mixing-limited combustion, as shown in Fig. 16. While both efficiencies are increasing, the increase is combustion efficiency is dictated by the increase in mixing efficiency. The final values for mixing and combustion efficiency are, respectively, 76% and 65%.

It is not possible to estimate the experimental mixing and combustion efficiencies with any degree of certainty from the simulation values. The rise in wall pressure in the experiment is too small at the fuelling rates used and the trips introduce considerable disturbances in the flow field which alter the shock train and pressure distribution, as seen in Fig. 7. The trips also considerably increase mixing as can be seen in the comparison with LES in Fig. 13. It is reasonable to assume the efficiencies are higher in the experimental case due to the trips, but not by how much.

C. Combustion regimes

To conclude the analysis of the supersonic combustion process, the combustion regimes need to be calculated. The methodology to calculate the parameters used in determining the regimes can be found in Section II.B.1.

The analysis begins with a determination of the combustion modes, i.e. premixed or non-premixed. This is done by evaluating the Takeno flame index (TFI) [54], defined as

$$TFI = \nabla Y_{O_2} \cdot \nabla Y_{H_2}. \tag{19}$$

A positive TFI indicates the angles of the vectors ∇Y_{O_2} and ∇Y_{H_2} are aligned, i.e. oxygen and hydrogen are coming from the same direction, therefore combustion is premixed. On the other hand, a negative value indicates ∇Y_{O_2} and ∇Y_{H_2} approach from opposite directions, characterising non-premixed combustion.

Figure 20 shows a heat map of the distribution of combustion regimes in the engine filtered by TFI. The diagram on the left contains all grid cells in which combustion is non-premixed, $TFI < -100$. The diagram on the right represents premixed combustion, $TFI \geq 100$. The values of TFI between ± 100 are excluded so that only cells with strong reactions are included. This excludes reactions involving only air species, which are not relevant to the combustion regimes. The n value under each plot is the number of grid cells in which either combustion mode is present. Most combustion is non-premixed, with around 5 million cells contributing to non-premixed combustion. Non-premixed combustion regimes are distributed over a large area of the diagram. There's a large distribution in the flamelet region, with a concentration in the boundary between flamelets and unsteady effects, according to the metrics we have used (see Section II.B). The distribution tends to higher Damköhler numbers, indicating fast chemistry. This agrees with the previous discussion regarding the flow being mixing-limited. Non-premixed combustion is also spread over a large range of Reynolds number, but with a higher concentration on lower $\log Re_t$, meaning the regions where non-premixed combustion happens are less turbulent. It can also be seen that non-premixed combustion shows to "hotter" regions on the map, one on the boundary between non-premixed flamelets and unsteady effects, and the other higher on the plot.

Premixed combustion, on the other hand, happens in just under 1 million cells. While there is less premixed combustion, its presence is not negligible and it cannot be said non-premixed combustion dominates the flow. Premixed combustion regimes are spread over a slightly smaller range of Damköhler numbers, most of it concentrated around a narrow region spanning $\log Da = 1$ to 4, while Reynolds numbers are concentrated on higher values, indicating stronger turbulence. The regimes are distributed over the flamelets and reaction zones regimes. Unlike non-premixed combustion which has two somewhat distinct regions in the heatmap, the distribution is more continuous.

Figure 21 shows contours of TFI in the engine. This allows investigation of where in the engine each combustion

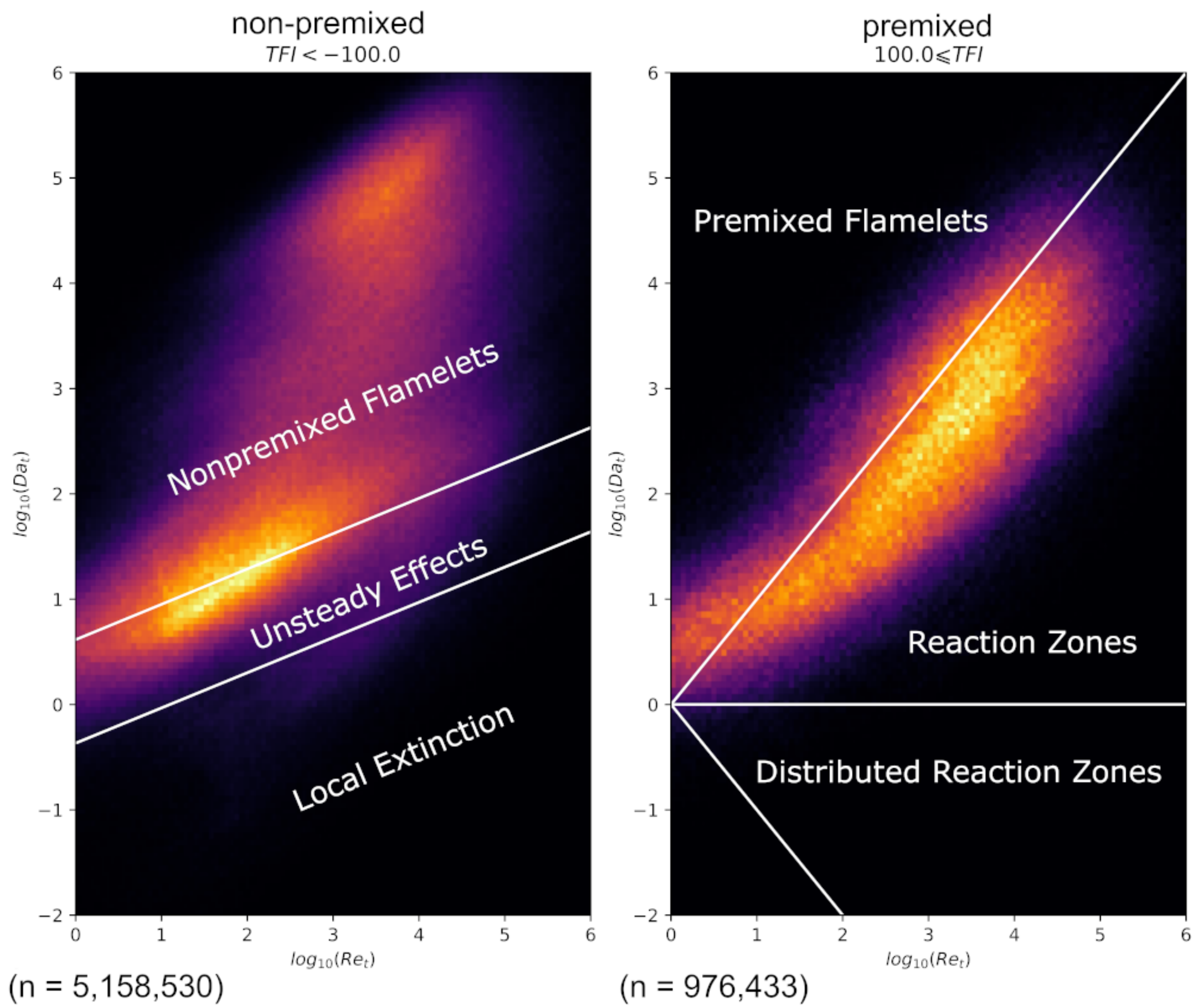

Fig. 20 Combustion regime diagram in the engine divided by combustion mode. Left is for non-premixed [55], right is for premixed [11] combustion.

mode takes place. Around the fuel plume, upstream of the combustor, TFI is almost completely negative, indicating the region is non-premixed. However, there are some small regions inside the fuel plume where TFI is positive, mainly close to the wall. This is likely due to mixing happening in the recirculation regions upstream and downstream of the injector [48], where fuel can get entrained and mixed with air. Inside the combustor, there is a premixed region that begins immediately downstream of the throat, close to the bottom wall. This region reduces in thickness until disappearing on the stream-wise plane after $x = 150$ mm. The premixed region persists entrained within the CVP up to $x = 200$ mm, after which there is negligible premixed combustion in the engine. The CVP therefore seems to considerably enhance mixing up to halfway through the combustor, as it retains unburned fuel long enough to properly mix it with surrounding air, even as the premixed region dwindles in the centre plane. Enveloping the premixed region is a layer of non-premixed combustion corresponding to the edge of the fuel plume. This layer persists through the entire combustor, becoming more distorted as the length scale of the turbulence increases as it moves downstream. Interestingly, the region where combustion starts to become premixed coincides precisely with the region where there is a reduction in the production rate of OH, seen in Fig. 18a. This could indicate that in the premixed region completion reactions are favored, consuming OH faster than it is produced. Further downstream, when the non-premixed region dominates, the production rate of OH increases again. Water seems unaffected by this. These results show that no single combustion mode exists exclusively in the flow. Combustion is initially non-premixed only, until a premixed region develops, likely due to shock/vortex interaction at the entrance of the combustor increasing the mixing rate. Both modes are present simultaneously in the first half of the combustor, after which combustion reverts to being non-premixed only. As discussed earlier, combustion seems to be mixing-limited in the engine (see Section IV.B). The TFI results give further indication of this, as non-premixed combustion is more present within the engine.

Finally, looking back Fig. 20, the spatial distribution of TFI helps explain the behaviour of non-premixed and premixed combustion in the heatmap. Premixed combustion exists in the engine as a continuous region, starting weakly close to the wall around the injector up to about halfway through the combustor. This can be seen in the continuous band in Fig. 20, with both Reynolds and Damköhler number increasing as the flow gets more turbulent and reactions accelerate. Non-premixed combustion, on the other hand, while present throughout the engine, clearly dominates upstream of the throat, and then on the second half of the combustor where premixed combustion is no longer present. These two regions could correlate to the stronger region with and unsteady effects and the second region higher up in Fig. 20, respectively. The second half of the combustor is more turbulent and hotter, which contributes to faster reactions (and higher Damköhler). On the other hand, the injector region is more unsteady as the injected fuel displaces the incoming flow and mixing begins around the fuel plume and the flow structures resulting from fuel injection.

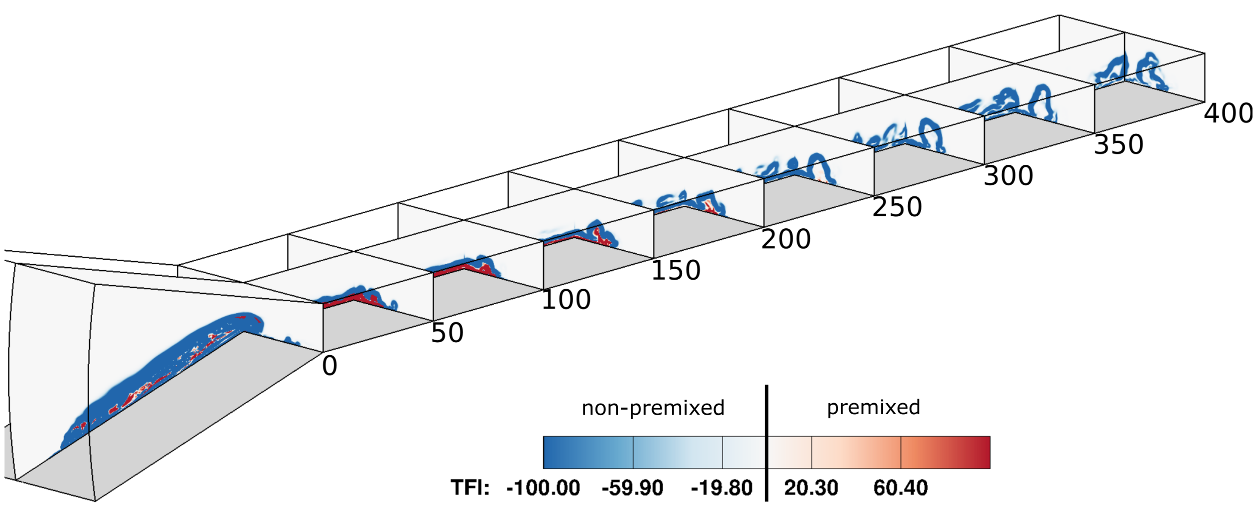

Fig. 21 Takeno flame index contours in the engine.

These results clearly demonstrate how complex the supersonic combustion process is in scramjet engines. Even though combustion is mixing-limited for most of the engine, there are regions of both premixed and non-premixed combustion, including regions where both happen simultaneously. The overall regime distribution is also complex. Both non-premixed and premixed combustion are distributed over multiple regimes.

V. Conclusion

Experimental and numerical results were analysed for an inlet-fuelled scramjet with flow enthalpy equivalent to Mach 10, and a fuel equivalence ratio of $\phi = 0.13$. Experimental results were obtained for wall pressure and the turbulent flame was observed directly using OH-PLIF imaging. These results indicate reactions begin early in the engine, with OH visible immediately downstream of the injector. As the flow progresses further downstream, it can be seen OH occupies a region that spans the height of the fuel plume, with turbulent structures clearly seen in the convoluted flame boundary. Turbulence is less visible on the flame towards the end of the combustor, most likely due to an increase in temperature leading to faster chemistry and more uniform OH distributions. Large-Eddy Simulations were performed using the experimental inflow conditions to provide better understanding of the flow features and characterise combustion. As the simulations didn't include a boundary-layer trip, mixing is slower than in the experimental testing. Nonetheless, good agreement is obtained when investigating a stream-wise plane offset by 3 mm from the center-plane. Numerical results show that the flow is quickly compressed as it enters the combustor, reaching conditions suitable for hydrogen autoignition. In this radical-seeded flow, there is initially fast production of water and OH. While OH production slows down, water increases consistently. This leads to consistent heat release in the engine, reaching a combustion efficiency of 65%. Combustion in the engine seems mixing-limited, and mixing efficiency reaches approximately 76% at the end of the combustor. The numerical results also indicate combustion is multi-mode, with non-premixed and premixed combustion both happening in the engine, either alternating or, in some regions, simultaneously. Non-premixed combustion is more prevalent, but not dominating. In terms of combustion regimes, according to the metrics we have employed, non-premixed combustion happens primarily in the flamelet and unsteady effects regimes, and premixed combustion happens over multiple regimes, most particularly flamelet and thick reaction zones. These results confirm that the combustion process in a scramjet engine, driven by its flow non-uniformities, is multi-mode and multi-regime.

Acknowledgments

The authors would like to thank the T4 team for support and operation of the facility: engineer Samuel Grieve, technician Keith Hitchcock, and operators Eric Wong, Jens Kunze, and Ryan Whitside. We'd also like to thank Tristan Vanyai for the support with the optics system prior to the experimental campaign. This work was completed with financial support from the Brazilian National Council of Scientific and Technological Development (CNPq) under grant 200515/2014-4. It was undertaken with the assistance of resources from the National Computational Infrastructure (NCI), which is supported by the Australian Government, and by resources provided by the Pawsey Supercomputing center with funding from the Australian Government and the Government of Western Australia.

References

[1] Segal, C., *The Scramjet Engine: Processes and Characteristics*, 1st ed., Cambridge University Press, Cambridge, 2009.

[2] Anderson, J. D., *Hypersonic and High Temperature Gas Dynamics*, McGraw-Hill series in aeronautical and aerospace engineering, American Institute of Aeronautics and Astronautics, 2006.

[3] Heiser, W. H., and Pratt, D. T., *Hypersonic Airbreathing Propulsion*, No. pt. 1 in AIAA Textbooks Series, American Institute of Aeronautics and Astronautics, 1994.

[4] Smart, M. K., "Scramjets," *RTO-EN-AVT-150*, 2008, pp. 1–38.

[5] Jazra, T., Preller, D., and Smart, M. K., "Design of an Airbreathing Second Stage for a Rocket-Scramjet-Rocket Launch Vehicle," *J. Spacecr. Rockets*, Vol. 50, No. 2, 2013, pp. 411–422. doi:10.2514/1.A32381.

[6] Forbes-Spyratos, S. O., Kearney, M. P., Smart, M. K., and Jahn, I. H., "Trajectory Design of a Rocket–Scramjet–Rocket Multistage Launch System," *Journal of Spacecraft and Rockets*, 2018, pp. 1–14. doi:10.2514/1.A34107, URL `https://arc.aiaa.org/doi/10.2514/1.A34107`.

[7] Doherty, L. J., Smart, M. K., and Mee, D. J., "Design of an Airframe Integrated 3D Scramjet and Experimental Results at a Mach 10 Flight Condition," *18th AIAA/3AF Int. Sp. Planes Hypersonic Syst. Technol. Conf.*, International Space Planes and Hypersonic Systems and Technologies Conferences, American Institute of Aeronautics and Astronautics, 2012. doi:doi:10.2514/6.2012-5910.

[8] Smart, M. K., and Tetlow, M. R., "Orbital Delivery of Small Payloads Using Hypersonic Airbreathing Propulsion," *J. Spacecr. Rockets*, Vol. 46, No. 1, 2009, pp. 117–125. doi:10.2514/1.38784.

[9] Bilger, R. W., Pope, S. B., Bray, K. N. C., and Driscoll, J. F., "Paradigms in turbulent combustion research," *Proceedings of the Combustion Institute*, Vol. 30, No. 1, 2005, pp. 21–42. doi:10.1016/j.proci.2004.08.273.

[10] Ingenito, A., and Bruno, C., "Physics and Regimes of Supersonic Combustion," *AIAA J.*, Vol. 48, No. 3, 2010, pp. 515–525. doi:10.2514/1.43652.

[11] Peters, N., *Turbulent Combustion*, Cambridge Monographs on Mechanics, Cambridge University Press, 2000. doi:10.1017/CBO9780511612701.

[12] Berglund, M., and Fureby, C., "LES of supersonic combustion in a scramjet engine model," *Proc. Combust. Inst.*, Vol. 31 II, 2007, pp. 2497–2504. doi:10.1016/j.proci.2006.07.074.

[13] Boyce, R. R., Mudford, N. R., and McGuire, J. R., "OH-PLIF visualisation of radical farming supersonic combustion flows," *Shock Waves*, Vol. 22, No. 1, 2012, pp. 9–21. doi:10.1007/s00193-011-0346-7.

[14] Cocks, P. A. T., Dawes, W. N., and Cant, R. S., "The Influence of Turbulence-Chemistry Interaction Modelling for Supersonic Combustion," *AIAA 2011-306*, 2011, pp. 1–12. doi:10.2514/6.2011-306.

[15] Drummond, J. P., Diskin, G. S., and Cutler, A. D., "Fuel Air Mixing and Combustion in Scramjets," *AIAA Pap. 2002-3878, 38 AIAA/ASME/SAE/ASEE Jt. Propuls. Conf. Exhib.*, AIAA, Indianapolis, Indiana, 2002, pp. 1–16.

[16] Gamba, M., Miller, V. A., Mungal, M. G., and Hanson, R. K., "Ignition and Flame Structure in a Compact Inlet/Scramjet Combustor Model," *17th AIAA International Space Planes and Hypersonic Systems and Technologies Conference*, 2011, pp. 1–23. doi:10.2514/6.2011-2366.

[17] Gamba, M., Miller, V., Mungal, G., and Hanson, R., "Combustion characteristics of an inlet/supersonic combustor model," *50th AIAA Aerospace Sciences Meeting including the New Horizons Forum and Aerospace Exposition*, , No. January, 2012. doi:10.2514/6.2012-612, URL `http://arc.aiaa.org/doi/10.2514/6.2012-612`.

[18] Johansen, C. T., McRae, C. D., Danehy, P. M., Gallo, E. C. A., Cantu, L. M. L., Magnotti, G., Cutler, A. D., Rockwell, R. D., Goyne, C. P., and McDaniel, J. C., "OH PLIF visualization of the UVa supersonic combustion experiment: Configuration A," *J. Vis.*, Vol. 17, No. 2, 2014, pp. 131–141. doi:10.1007/s12650-014-0197-2.

[19] Lorrain, P. M. C., "Flow Structure / Chemistry Coupling in the Ignition Process in Shock-Induced-Combustion Scramjets," Doctor of philosophy, University of Queensland, 2014.

[20] Smart, M. K., "Scramjet Inlets," *RTO-EN-AVT-185*, , No. 9, 2010, pp. 1–24.

[21] Llobet Gomez, J. R., "Numerical and Experimental Investigation of Hypersonic Streamwise Vortices and their Effect on Mixing," Doctor of philosophy, The University of Queensland, 2017.

[22] Gehre, R. M., "The Flow Physics of Inlet-Fueled , Low-Compression Scramjets," Doctor of philosophy, The University of Queensland, 2014.

[23] Stalker, R. J., "A study of the free-piston shock tunnel." *AIAA Journal*, Vol. 5, No. 12, 1967, pp. 2160–2165. doi:10.2514/3.4402, URL `http://arc.aiaa.org/doi/abs/10.2514/3.4402`.

[24] Doherty, L. J., "An Experimental Investigation of an Airframe Integrated Three-Dimensional Scramjet Engine at a Mach 10 Flight Condition," Doctor of philosophy, University of Queensland, 2014.

[25] Jacobs, P. A., Gollan, R. J., Potter, D., Zander, F., Gildfind, D., Blyton, P., Chan, W. Y. K., and Do, "Estimation of high-enthalpy flow conditions for simple shock and expansion processes using the ESTCj program and library." Tech. rep., The University of Queensland, Brisbane, Australia, 2014. URL `http://cfcfd.mechmining.uq.edu.au/pdf/estcj.pdf`.

[26] Gollan, R. J., and Jacobs, P. A., "About the Formulation, Verification and Validation of the Hypersonic Flow Solver Eilmer," *International Journal for Numerical Methods in Fluids*, Vol. 73, No. 1, 2013, pp. 19–57. doi:10.1002/fld.3790.

[27] Jacobs, P. A., Gollan, R. J., Denman, A., O'Flaherty, B., Potter, D. F., Petrie-Repar, P. J., and Johnston, I. A., "Eilmer's Theory Book : Basic Models for Gas Dynamics and Thermochemistry," Mechanical Engineering Report 2010/09, 2012.

[28] Barth, J. E., “Mixing and Combustion Enhancement in a Mach 12 Shape-Transitioning Scramjet Engine,” Phd, The University of Queensland, 2014.

[29] Landsberg, W. O., “Improving Performance of High Mach Number Scramjets : Fuelling Strategies and Combustor Design,” Ph.D. thesis, 2018.

[30] Vanyai, T., “Experimental Investigation of a 3D Thermal Compression Scramjet Using Advanced Optical Techniques,” Doctor of philosophy, The University of Queensland, 2018.

[31] Nompelis, I., Drayna, T. W., and Candler, G. V., “Development of a Hybrid Unstructured Implicit Solver for the Simulation of Reacting Flows Over Complex Geometries,” *34th AIAA Fluid Dyn. Conf. Exhib.*, American Institute of Aeronautics and Astronautics, 2004. doi:doi:10.2514/6.2004-2227.

[32] Peterson, D. M., “Simulations of Injection, Mixing, and Combustion in Supersonic Flow Using a Hybrid RANS/LES Approach,” Ph.D. thesis, University of Minnesota, 2011.

[33] Spalart, P. R., and Allmaras, S. R., “A one-equation turbulence model for aerodynamic flows,” *AIAA-92-G439*, 1992. doi:10.2514/6.1992-439.

[34] Allmaras, S. R., Johnson, F. T., and Spalart, P. R., “Modifications and Clarifications for the Implementation of the Spalart-Allmaras Turbulence Model,” *Seventh Int. Conf. Comput. Fluid Dyn.*, , No. July, 2012, pp. 1–11.

[35] Catris, S., and Aupoix, B., “Density corrections for turbulence models,” *Aerosp. Sci. Technol.*, Vol. 4, No. 1, 2000, pp. 1–11. doi:10.1016/S1270-9638(00)00112-7.

[36] Shur, M. L., Spalart, P. R., Strelets, M. K., and Travin, A. K., “A hybrid RANS-LES approach with delayed-DES and wall-modelled LES capabilities,” *International Journal of Heat and Fluid Flow*, Vol. 29, No. 6, 2008, pp. 1638–1649. doi:10.1016/j.ijheatfluidflow.2008.07.001.

[37] Spalart, P. R., Deck, S., Shur, M. L., Squires, K. D., Strelets, M. K., and Travin, A., “A new version of detached-eddy simulation, resistant to ambiguous grid densities,” *Theoretical and Computational Fluid Dynamics*, Vol. 20, No. 3, 2006, pp. 181–195. doi:10.1007/s00162-006-0015-0.

[38] Nikitin, N. V., Nicoud, F., Wasistho, B., Squires, K. D., and Spalart, P. R., “An approach to wall modeling in large-eddy simulations,” *Physics of Fluids*, Vol. 12, No. 7, 2000, pp. 1629–1632. doi:10.1063/1.870414.

[39] Spalart, P. R., “Strategies for Turbulence Modeling and Simulations,” *International Journal of Heat and Fluid Flow*, Vol. 21, No. 3, 2000, pp. 252–263. doi:10.1016/B978-008043328-8/50001-1.

[40] Gao, Z., Jiang, C., and Lee, C. H., “On the laminar finite rate model and flamelet model for supersonic turbulent combustion flows,” *Int. J. Hydrogen Energy*, Vol. 41, No. 30, 2016, pp. 13238–13253. doi:10.1016/j.ijhydene.2016.06.013.

[41] Barth, J. E., Wise, D. J., Wheatley, V., and Smart, M. K., “Tailored Fuel Injection for Performance Enhancement in a Mach 12 Scramjet Engine,” *20th AIAA Int. Sp. Planes Hypersonic Syst. Technol. Conf.*, 2015, pp. 1–37. doi:10.2514/1.B36794.

[42] Wilcox, D. C., *Turbulence modeling for CFD*, 3rd ed., DCW Industries, Incorporated, La Cañada, 1998.

[43] Lu, T. F., Yoo, C. S., Chen, J. H., and Law, C. K., "Three-dimensional direct numerical simulation of a turbulent lifted hydrogen jet flame in heated coflow: A chemical explosive mode analysis," *Journal of Fluid Mechanics*, Vol. 652, 2010, pp. 45–64. doi:10.1017/S002211201000039X.

[44] Landsberg, W. O., Gibbons, N. N., Wheatley, V., Smart, M. K., and Veeraragavan, A., "Improving Scramjet Performance Through Flow Field Manipulation," *Journal of Propulsion and Power*, 2017, pp. 1–13. doi:10.2514/1.b36772.

[45] Gibbons, N., Wheatley, V., and Doolan, C., "Preliminary Investigation of Sound Generation in Scramjets," *20th Australasian Fluid Mechanics Conference*, Perth, WA, Australia, 2016.

[46] Moura, A. F., Wheatley, V., and Jahn, I., "Thermofluidic compression effects to achieve combustion in a low-compression scramjet engine," *Shock Waves*, Vol. 28, No. 4, 2017, pp. 863–875. doi:10.1007/s00193-017-0782-0, URL https://doi.org/10.1007/s00193-017-0782-0.

[47] Moura, A. F., Gibbons, N., Wheatley, V., Mcintyre, T. J., and Jahn, I., "LES of oxygen enrichment in scramjet engines," *12th European Fluid Mechanics Conference*, EUROMECH, Vienna, Austria, 2018, p. 699.

[48] Génin, F., and Menon, S., "Dynamics of sonic injection into supersonic crossflow," *J. Turbul.*, , No. February 2014, 2010, p. N4. doi:10.1080/14685240903217813.

[49] Wise, D., "Experimental investigation of a three dimensional scramjet engine at hypervelocity conditions," Ph.D. thesis, 2015. doi:10.14264/uql.2015.465, URL http://espace.library.uq.edu.au/view/UQ:353779.

[50] Berry, S. A., Auslender, A. H., Dilley, A. D., and Calleja, J. F., "Hypersonic Boundary-Layer Trip Development for Hyper-X," *Journal of Spacecraft and Rockets*, Vol. 38, No. 6, 2001, pp. 853–864. doi:10.2514/2.3775, URL http://arc.aiaa.org/doi/10.2514/2.3775.

[51] Lee, S. H., "Characteristics of Dual Transverse Injection in Scramjet Combustor, Part 1: Mixing," *Journal of Propulsion and Power*, Vol. 22, No. 5, 2006, pp. 1012–1019. doi:10.2514/1.14185, URL https://arc.aiaa.org/doi/pdf/10.2514/1.14185.

[52] Mitani, T., and Kouchi, T., "Flame structures and combustion efficiency computed for a Mach 6 scramjet engine," *Combust. Flame*, Vol. 142, No. 3, 2005, pp. 187–196. doi:10.1016/j.combustflame.2004.10.004.

[53] Gehre, R. M., Peterson, D. M., Wheatley, V., and Boyce, R. R., "Numerical investigation of the mixing process in inlet-fuelled scramjets," *29th Int. Symp. Shock Waves*, 2013, pp. 1–7. doi:10.1007/978-3-319-16838-8_32.

[54] Yamashita, H., Shimada, M., and Takeno, T., "A numerical study on flame stability at the transition point of jet diffusion flames," *Symposium (International) on Combustion*, Vol. 26, No. 1, 1996, pp. 27–34. doi:10.1016/S0082-0784(96)80196-2.

[55] Veynante, D., and Vervisch, L., "Turbulent combustion modeling," *Prog. Energy Combust. Sci.*, Vol. 28, No. 3, 2002, pp. 193–266. doi:10.1016/S0360-1285(01)00017-X.